



Pitting mechanism of mild steel in marginally sour environments—Part I: A parametric study based on formation of protective layers

Wei Zhang ^{*},¹, Bruce Brown, David Young, Gheorghe Bota, Srdjan Nescic, Marc Singer

Institute for Corrosion and Multiphase Technology, Ohio University, 342 West State Street, Athens, OH, 45701, USA

ARTICLE INFO

Keywords:

- A. Mild steel
- B. Weight loss
- B. SEM
- B. TEM
- C. Acid corrosion
- C. Pitting corrosion

ABSTRACT

A parametric study defined a window of conditions leading to pitting of mild steel in marginally sour environments: temperatures between 30°C and 60°C, p_{H₂S} from 0.02 mbar to 0.15 mbar, bulk pH below 6, and sodium chloride concentrations between 1 and 10 wt. %. A 100–300 nm porous layer containing both mackinawite and magnetite was observed by transmission electron microscopy. Pitting initiated when the mackinawite layer was broken-down and exposed the steel surface to highly corrosive H₂CO₃. Pitting propagated due to the galvanic coupling between the exposed steel surface and the rest surface area covered by the conductive mackinawite.

1. Introduction

Localized corrosion is a common failure mode found in oil and gas pipelines containing carbon dioxide (CO₂), hydrogen sulfide (H₂S), and brine [1]. More specifically, issues with pitting corrosion in marginally sour environments have also been reported by the industry [2]. Researchers in the Institute for Corrosion and Multiphase Technology (ICMT) at Ohio University have previously reproduced localized corrosion in CO₂ environments with low concentrations of H₂S [3–7].

When investigating localized/pitting corrosion of steel, it is tempting to refer to the well-established theory of localized corrosion of stainless steel in an atmospheric environment (iron-oxygen-brine system), involving the disruption of the passive layer and pit acidification [8,9]. Passive layers are complicated structures on a nanometer scale [10], composed of oxides and hydroxides. However, these mechanisms cannot be applied to localized corrosion of mild steel in marginally sour environments containing both H₂S and CO₂ because the formation, structure and properties of the protective layer are completely different. Therefore, any mechanistic study of this phenomenon should begin with a systematic evaluation of the controlling operating factors and of layer characterization.

As depicted in Fig. 1, the localized corrosion mechanism is typically described as a three-step phenomenon: (i) protective layer formation; (ii) pit initiation (nucleation); (iii) pit propagation or annihilation. The characteristics of the protective layers are thought to govern whether or

not localized corrosion will occur and to determine what mechanisms are involved. Therefore, layer growth mechanisms, kinetics, morphology, and phase identity constitute a major focus of the present localized corrosion study.

Layers formed on the surface of mild steel in marginally sour environments might contain iron carbonate (FeCO₃), iron sulfide (Fe_xS_y), iron carbide (Fe₃C) and possibly iron oxides (Fe_xO_y). Knowledge on FeCO₃ and Fe_xS_y corrosion product layer growth mechanisms has been accumulating over several decades of systematic research on CO₂ and H₂S corrosion. The key points are summarized in Table 1. For FeCO₃, it is understood that the layer is formed by precipitation [11], as shown by reaction (1). The driving force for precipitation is the degree of saturation of FeCO₃ in aqueous solution [12]. FeCO₃ precipitates when saturation degree is greater than unity, as shown by reaction (4). The layer growth rate is related to the activation energy and the aforementioned degree of saturation, as shown by reaction (6). This corrosion product layer can be “undermined” by corrosion of the underlying steel, if the ratio of precipitation to corrosion rates is near or less than unity, in line with equation (8). This “undermining effect” was proposed as an initiation mechanism for localized corrosion in sweet (CO₂ only) environments [12].

Corrosion products in sour environments contain at least one polymorph of iron sulfide, such as mackinawite (FeS), pyrite (FeS₂), pyrrhotite (Fe_(1-x)S, x = 0 ~ 0.2), or greigite (Fe₃S₄), depending on environmental conditions such as temperature and p_{H₂S}, as well as

* Corresponding author.

E-mail address: wz521414@ohio.edu (W. Zhang).

¹ 7669 State Route 56, Athens, OH, 45701, USA.

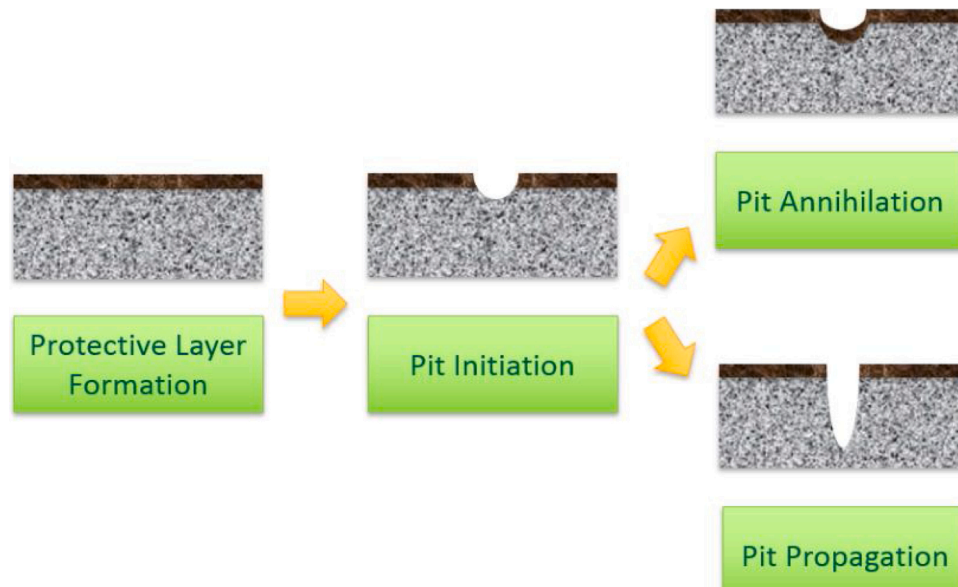


Fig. 1. Schematic representation of the three steps of localized corrosion.

Table 1
FeCO₃ Layer and FeS Layer Growth Mechanisms.

| | In CO ₂ Corrosion (by precipitation) | In H ₂ S Corrosion (by precipitation) | In H ₂ S Corrosion (by chemisorption) |
|-------------------------------|--|--|--|
| Layer Formation | $Fe_{(aq)}^{2+} + CO_3^{2-} \rightarrow FeCO_3(s) \downarrow$ (1) | $Fe_{(aq)}^{2+} + H_2S_{(aq)} \leftrightarrow FeS_{m(s)} \downarrow + 2H_{(aq)}^+$ (2) | $H_2O_{ads}(Fe) + H_2S_{(aq)} \rightarrow S_{ads}(Fe) + H_2O_{(l)} + 2H_{(aq)}^+ + 2e^-$ (3) |
| When does the layer form? | $S_{FeCO_3} = \frac{[Fe^{2+}][CO_3^{2-}]}{k_{sp,FeCO_3}} > 1$ (4) | $S_{FeS} = \frac{[Fe^{2+}][HS^-]}{k_{sp,FeS}[HS^-]} > 1$ (5) | When H ₂ S chemisorbs on the steel surface |
| How fast does the layer form? | $PR_{FeCO_3(s)} = e^{\frac{28.2 - 64851.4}{RT} S} \frac{S}{\sqrt{V}} k_{sp,FeCO_3} (S_{FeCO_3} - 1)$ (6) | $PR_{FeS(s)} = e^{\frac{48. - 40000}{RT} S} \frac{S}{\sqrt{V}} k_{sp,FeS} (S_{FeS} - 1)$ (7) | Almost instantaneous when H ₂ S present |
| Is this layer protective? | Can act as a diffusion barrier depending on scaling tendency $ScalingTendency = \frac{PrecipitationRate}{CorrosionRate}$ (8) | Can act as a diffusion barrier depending on scaling tendency | Yes - decreases the rate of electrochemical reactions |

Where S_{FeCO_3} stands for saturation degree of FeCO₃; S_{FeS} stands for saturation degree of FeS (mackinawite); $k_{sp,FeCO_3}$ stands for equilibrium constant of FeCO₃; $k_{sp,FeS}$ stands equilibrium constant of FeS (mackinawite); $PR_{FeCO_3(s)}$ stands for the precipitation rate of FeCO₃; $PR_{FeS(s)}$ stands for the precipitation rate of FeS (mackinawite); $\frac{S}{\sqrt{V}}$ stands for surface volume ratio.

exposure time, although there are different mechanisms proposed for their formation/transformation [13]. It is thought that mackinawite is always the initial FeS corrosion product [14] and that it is then converted into other forms of iron sulfide. Sun and Nescic [15] proposed a mechanism of iron sulfide layer formation at the steel surface by direct reaction between H₂S and the iron in the steel, forming a thin layer that spalls and reforms, to produce a thicker outer layer of iron sulfide. Zheng et al. further developed the “two layers” theory of iron sulfide formation and proposed that the inner layer forms by chemisorption [16], as previously postulated by others [17,18] [reaction (3)], while the outer layer forms by precipitation [16] [reaction (2)]. The chemisorbed layer is also considered to be very thin; of the order of nanometers (supposed to be single atom layer). The outer precipitated layer of FeS can be found

on top of the chemisorbed layer, its formation being driven by the saturation degree of Fe²⁺ and S²⁻ in the aqueous solution near the steel surface [equation (5)] [16]. The precipitated layer thickness is usually measured on a micron scale, and its growth rate can be defined via precipitation kinetics [18,19] [equation (7)]. The exact role of different iron sulfides in corrosion protection and pit initiation/propagation is poorly understood. One type of localized corrosion in sour environments was found to be related to pyrite [20–22] and pyrrhotite [23], which usually appears in H₂S dominant environments. In actuality, most of the research found in the open literature was done in H₂S dominant environments, often without CO₂. In addition, research on structure and morphology of the corrosion product layers related to localized corrosion in marginally sour environments is scarce.

Table 2
Key concepts of “grey zone” theory.

| $S_{FeCO_3} < 1$ | $S_{FeCO_3} \approx 1$ | $S_{FeCO_3} \gg 1$ |
|------------------------|----------------------------|------------------------|
| No layer | Partially protective layer | Fully protective layer |
| High uniform corrosion | Low/High uniform corrosion | Low uniform corrosion |
| No localized corrosion | Localized corrosion | No localized corrosion |



Fig. 2. Using the concept of scaling tendency to describe pit initiation in CO₂ environments by undermining effect.

Table 3

Chemical composition (wt. %) of API 5 L X65.

| Fe% | Mn% | Ni% | Cr% | Cu% | Si% | Mo% | C% |
|---------|--------|--------|--------|--------|--------|--------|---------|
| 97.3237 | 1.5052 | 0.2909 | 0.2519 | 0.1731 | 0.1668 | 0.0921 | 0.0454 |
| V% | Nb% | Al% | Ti% | As% | N% | S% | Others% |
| 0.0420 | 0.0338 | 0.0282 | 0.0120 | 0.0075 | 0.0067 | <0.001 | 0.0136 |

Another constituent of the corrosion product layer is often iron carbide (also called cementite), Fe₃C, which is a component of the steel microstructure. Since it does not readily corrode, it remains as a residue on the steel surface after the ferrite (α -Fe) phase is dissolved, the same being true in marginally sour environments. Corrosion products such as FeCO₃ and iron sulfide can precipitate within the exposed Fe₃C network, due to the higher S_{FeCO_3} or S_{FeS} brought by the mass transfer barrier effect of Fe₃C network, thus making it an important constituent of the protective surface layers in sour corrosion.

Iron oxides might be found together with FeCO₃ and/or Fe_xS_y due to higher surface pH [24], reactions with oxygen [25], or from water at elevated temperature [20,22].

In CO₂ corrosion, the protective layer is FeCO₃, often presenting within the Fe₃C network. The loss of integrity of this layer has been linked to the occurrence of localized corrosion. Since the FeCO₃ layer is formed by precipitation, it is driven by the saturation degree of FeCO₃ in the solution. Therefore, the possibility of pitting can be predicted by the saturation degree of FeCO₃ (the grey zone theory [12], Table 2), as well as the rate of layer growth compared with the corrosion rate (scaling tendency [26], Fig. 2). Iron oxides have been found underneath the FeCO₃ layer and were linked to an increase of potential and development of localized corrosion [27].

Based on these findings in CO₂ corrosion, a similar hypothesis can be proposed for localized corrosion of mild steel in marginally sour environments. Since adding H₂S into a CO₂ environment leads to lower uniform corrosion rates, the formation of a FeS layer could be speculated to be more protective than the formation of an FeCO₃ layer. Therefore, saturation degree and scaling tendency of FeS can be used to predict if a protective layer of FeS is precipitated on a steel surface. The central hypothesis of this research is: “in a marginally sour environment, localized corrosion is initiated and sustained when a partially protective corrosion product layer is formed”.

In this work, a comprehensive parametric study was performed using a small-scale laboratory setup with the aim of changing the saturation degree of FeS and FeCO₃ by changing these conditions and filtering out the most influential factors of pitting in marginally sour environments. The parameters of interest were partial pressure of H₂S, bulk pH, temperature, the partial pressure of CO₂, and salt concentration. These series of experiments defined a window of operating conditions leading to the occurrence of pitting, and enabled the characterization of the corrosion product layer structure as well as the identification of the mechanisms related to the initiation of pitting in marginally sour environments.

2. Experimental setup and procedure

2.1. Experimental materials

API 5L X-65 mild steel [28] was chosen as the baseline steel type for this research due to its wide application in oil and gas pipelines. The

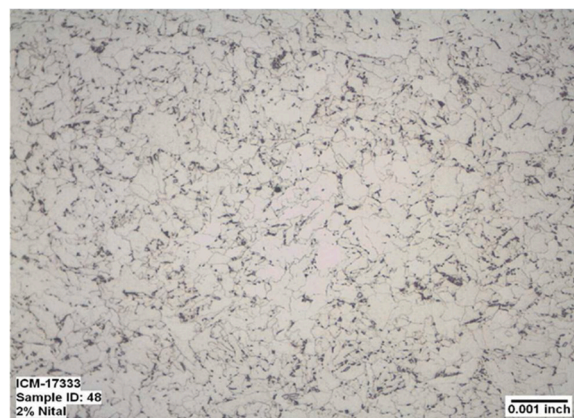


Fig. 3. Microstructure of X65 (0.05 wt. % C) consisting of large ferrite grains with cementite precipitates.

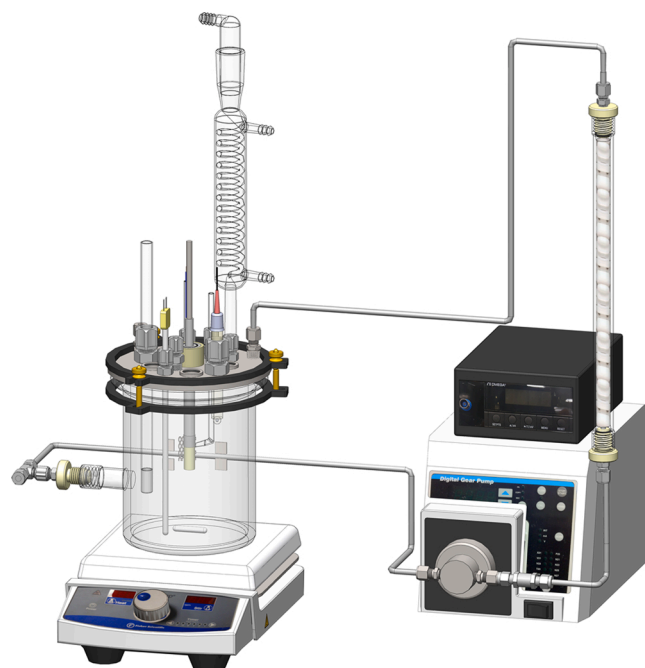


Fig. 4. Experimental setup for the two-liter glass cell using a stable solution chemistry system for small-scale experiments (Image courtesy of Cody Shafer, ICMT).

Table 4Test matrix of the parametric study ($P_{\text{total}} = 1$ bar, $[\text{O}_2]_{\text{aq}} \approx 20$ ppb_(w), stir bar rotation speed = 300 rpm).

| | Baseline | pH ₂ S*/mbar | pCO ₂ **/bar | Solution pH | Temperature/°C | NaCl wt. % |
|----------------------------|----------|----------------------------|-------------------------|-------------|----------------|--------------|
| Temperature/°C | 30 | 30 | 30 | 30 | 60, 80 | 30 |
| pH | 5 | 5 | 5 | 4, 6 | 5 | 5 |
| pCO ₂ /bar | 0.97 | 0.97 | 0, 0.53, 0.82 | 0.97 | 0.82, 0.53 | 0.97 |
| pH ₂ S/mbar | 0.04 | 0, 0.02, 0.09, 0.15 | 0.04 | 0.04 | 0.03, 0.02 | 0.04 |
| pH ₂ S/ppm | 40 | 0, 20, 90, 150 | 40 | 40 | 40 | 40 |
| WE Material | X65 | X65 | X65 | X65 | X65 | X65 |
| NaCl Concentration/ (wt.%) | 1 | 1 | 1 | 1 | 1 | 0, 10 |
| Exposure Time/day | 7 | 7 | 7 | 7 | 7 | 7 |
| Corrosion rate | | | | | | |

* Partial pressure of H₂S in the gas phase.** Partial pressure of CO₂ in the gas phase.

composition of the steel is shown in Table 3 [29]. Its microstructure consists of large ferrite grains with small precipitates of cementite. Pearlite colonies are difficult to be identified due to the low carbon content, as shown in Fig. 3 [30]. The cylindrical working electrode was machined from the parent steel material and had a diameter of 1.20 cm and an exposed surface area of 5.4 cm². The steel specimens were obtained from a large piece of pipe provided by a major oil and gas company. The composition and microstructure are believed to be representative of materials used in production and transportation of hydrocarbon products.

2.2. Experimental equipment

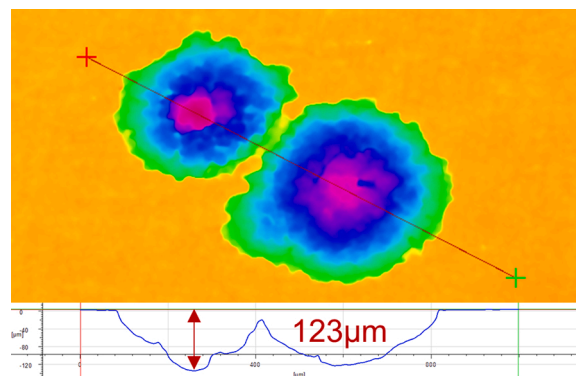
Experiments were conducted at atmospheric pressure in a 2-liter glass cell (Fig. 4 [31]) with a 1 wt. % NaCl in deionized water solution. Gas (a mixture of hydrogen sulfide, H₂S and carbon dioxide, CO₂) was sparged through the cell continuously at a flow rate of around 100 mL/min. A three-electrode electrochemical setup was used and consisted of: a static cylindrical electrode as the working electrode (WE), a platinum wire as a counter electrode (CE), a saturated silver-silver chloride (Ag|AgCl) reference electrode (RE) connected to the cell externally via a salt bridge with a Luggin capillary. A 2" magnetic stir bar at the bottom of the glass cell was used for mixing the solution. The concentration of H₂S was adjusted with the help of a gas rotameter and measured when exiting the cell by a gas sampling pump with H₂S colorimetric detector tubes. A carbon scrubber was used to treat the gas coming out of the glass cell to remove the H₂S. Automatic adjustment of pH over time was achieved by using the measured pH value to control a pump moving a part of the solution through an ion exchange resin column.

2.3. Experimental matrix

The test matrix (Table 4) was designed to develop an experimental database to screen the most influential factors of pitting in marginally sour environments. The following parameters were investigated: pH₂S, pCO₂, pH, temperature, and salt concentration. The choice of numerical values selected for each of these parameters is based on what is typically experienced in field applications and on previous laboratory experimental work. The core idea of these designed experiments involving various factors is to use the changes of saturation degree to predict the structure and properties of corrosion product layers, then correlate the layer protectiveness with the initiation of pitting.

2.4. Experimental procedure

The aqueous solution was initially sparged with CO₂ gas for at least two hours to purge dissolved oxygen. An oxygen meter (Hach® Orbisphere 510) was used to monitor the dissolved oxygen concentration inside the solution. Usually, two hours of sparging could bring down the $[\text{O}_2]_{\text{aq}}$ from 8 ppm_(w) to 10 ppb_(w), although it could fluctuate and

**Fig. 5.** Optical profilometry measurement.

increase to 20 ppb_(w) at the end of the seventh day. After the solution was deoxygenated, H₂S was added by sparging for about half an hour to saturate the solution. H₂S gas concentration was adjusted by sparging different ratios of CO₂ and H₂S, from 20 ppm_(v) to 150 ppm_(v), corresponding to a H₂S partial pressure $p_{\text{H}_2\text{S}} = 0.02$ mbar to 0.15 mbar respectively, at 30 °C. The pH value was adjusted by adding a deoxygenated hydrochloric acid or sodium carbonate aqueous solution. Prior to immersion, the mild steel specimen surfaces were polished with 80, 400 and 600 grit sandpaper, rinsed with isopropyl alcohol, and dried with an air blower.

Four X65 steel coupons of dimension of around 12.7 × 12.7 × 2 mm³ were used as the weight loss specimens during the corrosion experiments. One corroded specimen would be retrieved after one day, three days of experiment, then the rest two coupons (one for SEM cross section image) were retrieved after seven days exposure. The weight loss measurement was implemented according to the ASTM G1-2017 *Standard Practice for Preparing, Cleaning, and Evaluating Corrosion Test Specimens*.

Scanning electron microscopy (SEM, JEOL JSM-6390) and energy dispersive X-ray spectroscopy (EDS) were used to analyze the corrosion product layer structure and elemental composition.

Specimens from selected conditions were analyzed by transmission electron microscopy (TEM). Sections were cut from the scale with a FEI Nova Nanolab 200 FEG-SEM/FIB for Focused Ion Beam (FIB) processing and imaged with a FEI Tecnai F30 ST TEM. Both SEM and TEM were combined with EDS to analyze the chemical composition of the surface layers. The identity of crystalline components of the layers was revealed by selected area electron diffraction (SAED). The selected points in the corrosion product layer were further probed by precession electron diffraction (PED) to determine the crystal structures of specimen surface.

Pit penetration rate and pitting density were measured by scanning the steel surface after the corrosion product layer was removed, using a high-resolution optical profilometer, according to ASTM G 46 - 94 (2018) *Standard Guide for Examination and Evaluation of Pitting Corrosion*.

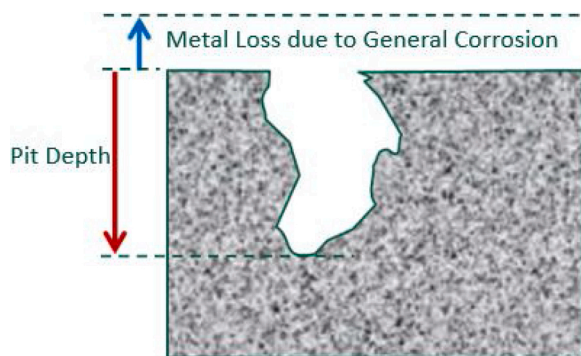


Fig. 6. Pit depth and general corrosion.

Surface profilometry scanning on corroded specimen surface was performed on the Alicona InfiniteFocus profilometer microscope. Fig. 5 shows an example of optical profilometry measurements that were used to identify the maximum pit depth. The measured three-dimensional nature of the pit is illustrated here by using a color scale, where the maximum depth is shown in the line profile below.

2.5. Evaluation of pitting ratio

Based on the ASTM G 46 – 94(2018), a rule has been developed to help decide whether localized corrosion occurred or not in the present experiments [32]. As demonstrated in Fig. 6, when exposed to the corrosive environment, steel specimens suffer from both general metal loss and localized attack. General corrosion rate could be calculated from total mass loss (here weight loss corrosion rate was used, denoted as CR_{WL} hereafter, Eq. (9), assuming that the contribution of pitting is negligible. The rate of localized attack could be evaluated by profilometry using the maximum pit depth (Eq. (10)), denoted as pit penetration rate (PPR) hereafter. The ratio of PPR divided by CR_{WL} is defined as pitting ratio (denoted as PR hereafter) and is used as the criteria for determining the occurrence of localized corrosion (Eq. (11)).

The rule is as follows: when this ratio is:

- A Smaller than 3, the corrosion is judged to be uniform;
- B Larger than 5, it is judged that localized corrosion occurred;
- C Between 3–5, the situation is unclear, it is possible that localized corrosion initiated but could not be sustained.

This criterion was only applied to pits that are deeper than 10 μm in order to distinguish them from general surface roughening.

$$\text{WeightLossCorrosionRate} \left(\frac{\text{mm}}{\text{y}} \right) = \frac{\text{MeasuredWeightLoss}}{\text{Time}} \quad (9)$$

$$\text{PenetrationRate} \left(\frac{\text{mm}}{\text{y}} \right) = \frac{\text{MeasuredPitDepth}}{\text{Time}} \quad (10)$$

$$\text{PittingRatio} = \frac{\text{PenetrationRate}(\text{mm/y})}{\text{WeightLossCorrosionRate}(\text{mm/y})} \quad (11)$$

2.6. Repeatability of the experiments

All the experiments listed in the test matrix have been repeated at least one more time using the same procedures and evaluation methodologies. Because these are long-term experiments (7 days), usually more trials were needed in order to achieve at least two repeatable results. The numerical results presented in this paper were the average of the two repeatable results, while the image results are just one set chosen from the two. Since this paper is on the occurrence of pitting, the criterion of repeatability is that pitting always occurs under certain conditions, but never occurred under other conditions.

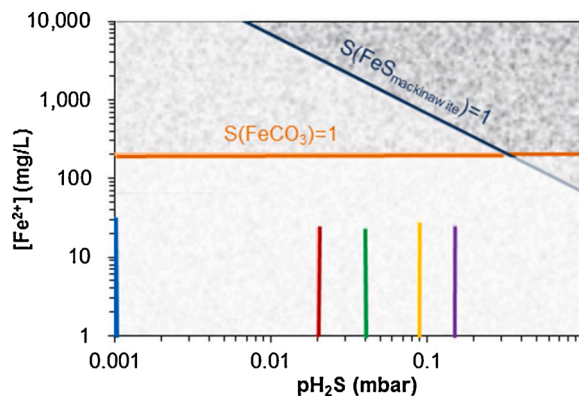


Fig. 7. Saturation degree of the bulk solution of both $\text{FeS}_{\text{mackinawite}}$ and FeCO_3 for different pH_2S values. (X65 carbon steel, 30 °C, pH 5, $\text{pCO}_2 = 0.97$ bar, $\text{pH}_2\text{S} = 0/0.02/0.04/0.09/0.15$ mbar, 1 wt.% NaCl, 300 rpm stir bar, 7 days exposure, $[\text{O}_2]_{\text{aq}} \approx 20$ ppb_(w)).

2.7. Experimental safety

Occupational Safety and Health Administration (OSHA), US Department of Labor, states that the immediate danger to life and health limit (IDLH) for H_2S gas is 100 ppm [33]. For this work, it is required to carry out all experiments following the ICMT protocol for working with H_2S gas. All staff and students are trained before using the specially equipped H_2S room at the ICMT. Personal working in the room is equipped with a self-contained breathing apparatus (SCBA). There is always a buddy outside the room watching activities and he/she is equally equipped. The H_2S in the outlet gas is scrubbed through a series of scrubbers that prevents its release to the atmosphere.

3. Results and discussion

The core idea of the designed experiments is to use changes of saturation degree to predict the morphologies and properties of corrosion product layers, then correlate the layer protectiveness with the initiation of pitting.

3.1. Effect of H_2S partial pressure on pitting

Experimental results obtained with 0, 20, 40, 90 and 150 ppm of H_2S in 1 bar CO_2 and at 30 °C were compared to identify the lower and upper limits of H_2S for localized corrosion occurrence. Fig. 7 shows the bulk saturation degree calculated for both FeS (mackinawite in this work), FeS , and FeCO_3 , S_{FeCO_3} under these conditions. The calculation method is explained in the modeling paper published previously in the same institute [34]. The navy line is the saturation line for FeS and shows the conditions required, in terms of $[\text{Fe}^{2+}]$, to reach saturation $S_{\text{FeS}} = 1$ at a given H_2S partial pressure. The orange line is the calculated saturation limit for $\text{FeCO}_3 - S_{\text{FeCO}_3}$. The corresponding corrosion product layer (FeS and/or FeCO_3) is expected to form by precipitation at any point in this chart above the saturation lines. During each experiment at a specific H_2S partial pressure, the measured bulk ferrous ion concentration started at zero at the beginning of the experiment, and then increased and reached a stable value, usually after 4 days of exposure, as indicated by the colored vertical lines in Fig. 7. In all five experiments, the bulk ferrous ion concentration did not reach the saturation value for either S_{FeS} or S_{FeCO_3} . Therefore, no precipitated layer would be expected in any of these experiments based on bulk water chemistry conditions.

Surface profilometry images of the corroded specimens, after corrosion product layer removal by Clarke solution, are displayed in Fig. 8. According to the criterion for pitting defined by Brown [32], the specimens exposed to 20, 40 and 90 ppm_(v) H_2S clearly experienced pitting. The pitting density for the 90 ppm_(v) H_2S was much lower than

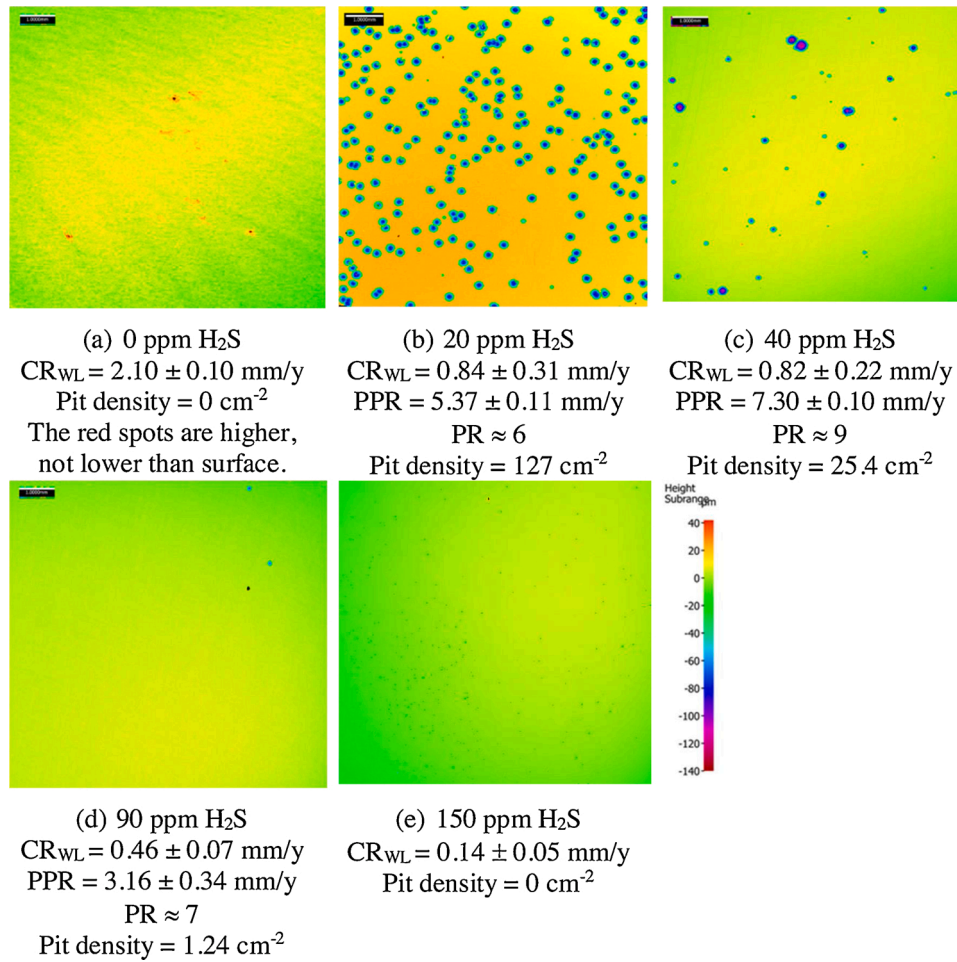


Fig. 8. Surface profilometry analysis of specimens recovered for each experimental condition after 7 days exposure after corrosion product layer removed. (X65 carbon steel, 30 °C, pH 5, pCO₂ = 0.97 bar, pH₂S = 0/0.02/0.04/0.09/0.15 mbar, 1 wt.% NaCl, 300 rpm stir bar, [O₂]_{aq} ≈ 20 ppb_(w)). The scales of the surface height of the three images were deliberately kept the same.)

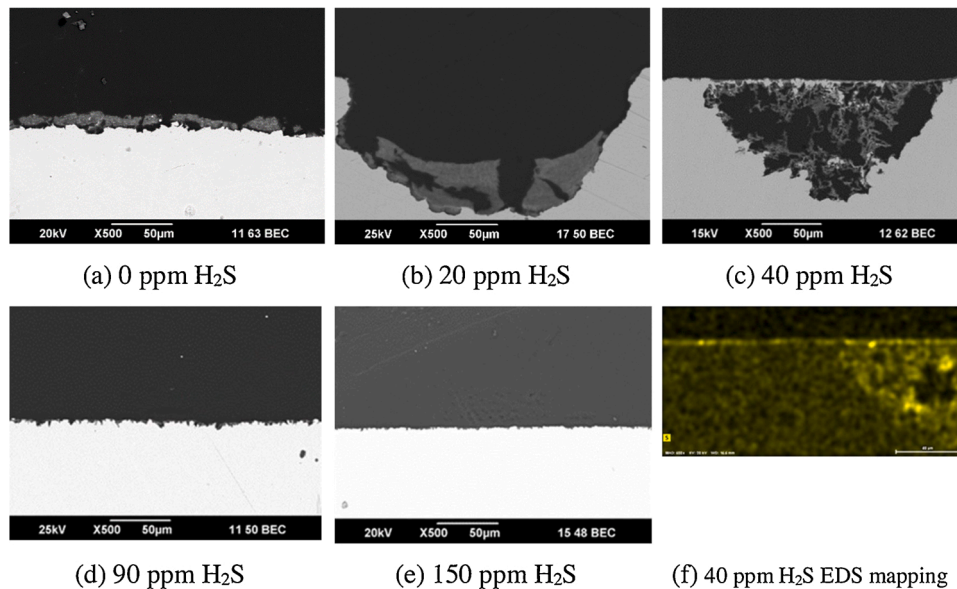


Fig. 9. SEM cross-section images of specimens at different H₂S partial pressure after 7 days exposure. (X65 carbon steel, 30 °C, pH 5, pCO₂ = 0.97 bar, pH₂S = 0/0.02/0.04/0.09/0.15 mbar, 1 wt. % NaCl, 300 rpm stir bar, 7 days exposure, [O₂]_{aq} ≈ 20 ppb_(w)).

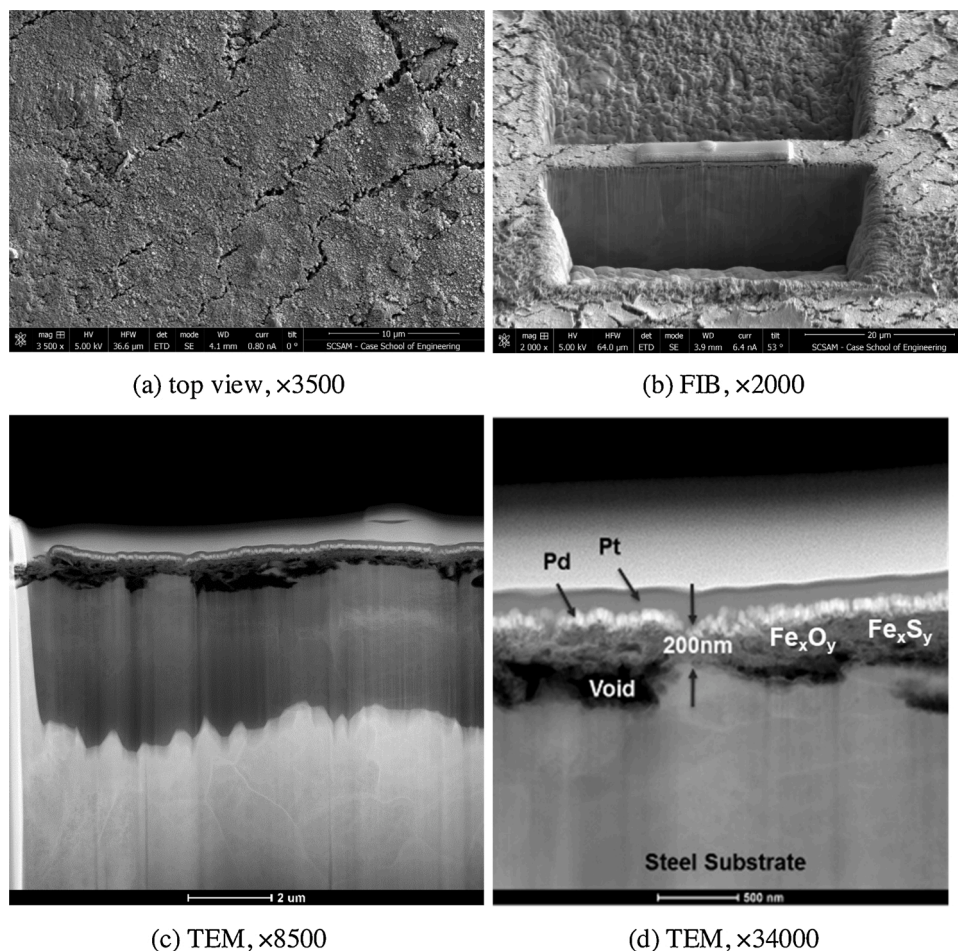


Fig. 10. TEM images of the cross section of the specimen for the baseline experiment cut out by FIB (30 °C, $p_{\text{CO}_2} = 0.97$ bar, $p_{\text{H}_2\text{S}} = 0.04$ mbar, pH 5, X65, 1 wt.% NaCl, 300 rpm, 7 days, $[\text{O}_2]_{\text{aq}} \approx 20$ ppb_(w)).

what was observed for 20 and 40 ppm_(v). However, according to the ASTM G46 – 94(2018), this pitting density was actually very high when compared to the threshold listed in the standard. Generally, the pitting density seemed directly related to H₂S concentration. High pitting density was observed at 20 ppm and 40 ppm H₂S. Lower pitting density was observed at 90 ppm H₂S. No pitting was found at 0 and 150 ppm H₂S. It seems therefore that there is a threshold of H₂S content for this type of pitting, indicating that the corrosion product layer became more stable as iron sulfide content increased, and was fully formed at 150 ppm H₂S since no pitting was observed. If this layer was formed by precipitation, it can be speculated that the surface saturation degree of FeS must have been greater than unity, even though the bulk value was not.

Fig. 8 shows the pitting analysis and compares it to the general corrosion rates determined by weight loss. The error margins for the general corrosion rate listed in the captions of Fig. 8 were calculated as follows: each experiment was repeated, so the reported (general) corrosion rate is the average values for the two specimens. The error margins denote the minimum and maximum measured values. The pit penetration rate reported there was based on the deepest pit found on the two specimens from repeated experiments. The margin of error reported for the pit penetration rate is calculated based on the vertical resolution of the optical measurements. LPR corrosion rates are available in the author's dissertation retrievable through open source via OhioLink [35].

According to Fig. 8, the CO₂ only (0 ppm H₂S) experiment yielded the highest general corrosion rate, ca. 2–2.5 mm/y. Adding 20 ppm of H₂S led to a considerable reduction in the general corrosion rate to less than 1.0 mm/y, although severe pitting would be expected to affect the

calculations. In general, the higher the H₂S content in the gas phase was, the lower the general corrosion rates became. The reason for the decrease in corrosion rate has been attributed in the literature to the formation of a thin FeS layer on the steel surface, although the bulk conditions were unfavorable for the precipitation of corrosion products. This trend indicates that the FeS layer (not FeCO₃, Fe₃C or Fe₂O₃ if they also existed in the layer) offers protection against corrosion in marginally sour environments. This observation fulfills one aspect of the “grey zone” theory, which requires the formation of a protective layer. For the hypothesis to be verified, the occurrence of pitting should be linked to breakdown of this FeS layer.

SEM images in Fig. 9 (a) reveal that in the absence of H₂S, a relatively thick layer was formed while no visible layer was found for the other cases with H₂S (this observation is limited by the resolution of the SEM). More importantly, Fig. 9 (b) and (c) indicate that extensive pitting occurred with 20 and 40 ppm H₂S but not in the other conditions [(d) and (e)]. This is consistent with the findings of Navabzadeh [3]. The cross-section images also show the morphology of those pits, which seem to be mainly hemispherical and filled with FeS embedded in a Fe₃C network. A thin layer (most likely FeS) was left behind at the top of the pit [Fig.9 (c)]. However, the resolution of these SEM images is insufficient to determine whether the thin layer exists on the remaining steel surface around the pits. It is thought that a very thin iron sulfide corrosion product layer (not visible in the SEM images) existed because sulfur was detected by EDS there [Fig. 9 (f)], which is also true for similar experiments conducted previously [3]. XRD failed to show a pattern or peaks to support this speculation because the layer was too thin to be properly resolved [3].

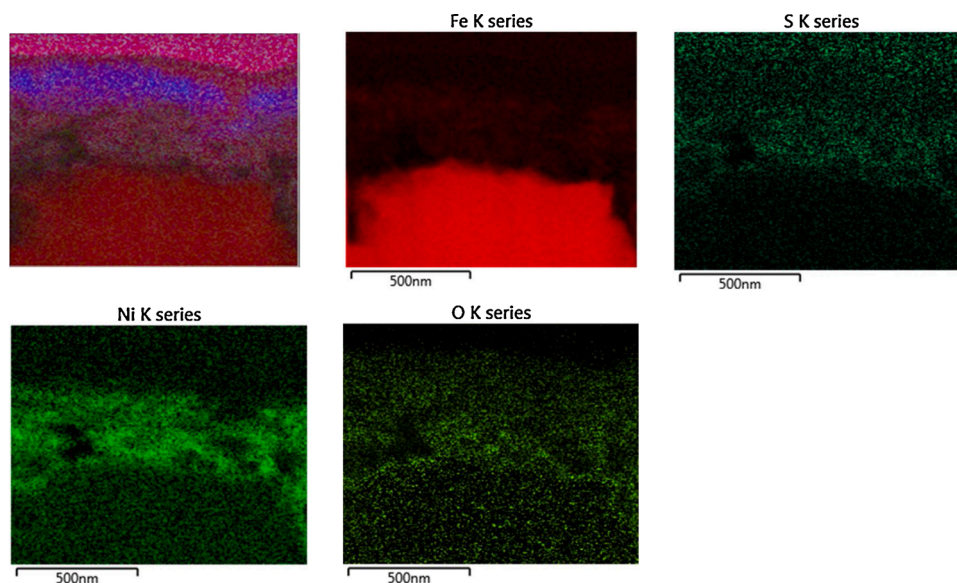


Fig. 11. TEM-EDS mapping results of the specimen of baseline condition experiment. (30 °C, $p_{\text{H}_2\text{S}} = 0.04$ mbar, $p_{\text{CO}_2} = 0.97$ bar, X65 carbon steel, pH 5, 1 wt.% NaCl, 300 rpm, 7 days, $[\text{O}_2]_{\text{aq}} \approx 20$ ppb_(w)).

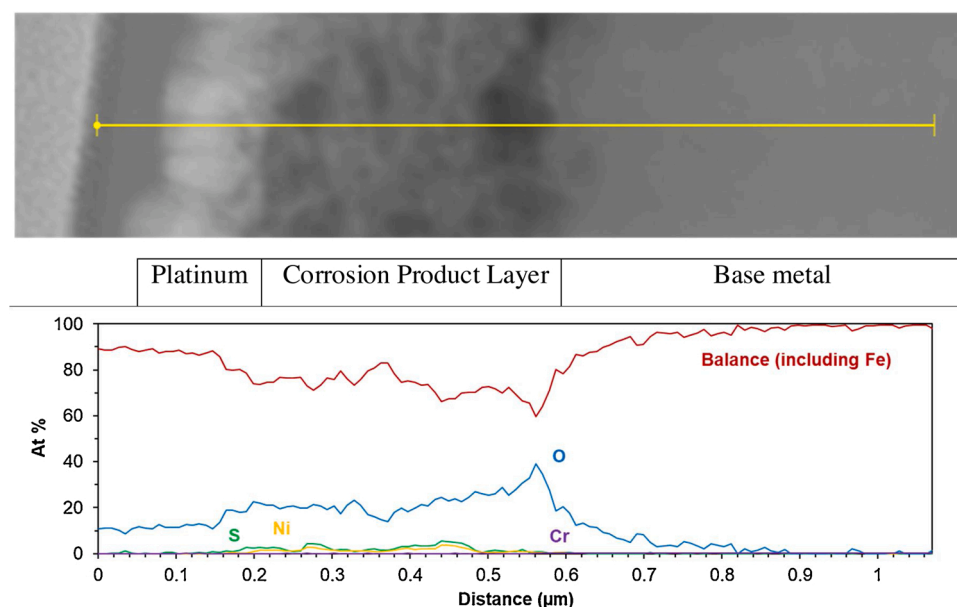


Fig. 12. TEM-EDS line scan results of the specimen in baseline condition. (30 °C, $p_{\text{H}_2\text{S}} = 0.04$ mbar, $p_{\text{CO}_2} = 0.97$ bar, X65 carbon steel, pH 5, 1 wt.% NaCl, 300 rpm, 7 days, $[\text{O}_2]_{\text{aq}} \approx 20$ ppb_(w)).

The 40 ppm H_2S specimen, where the most severe pitting happened in this series, was chosen for FIB-TEM analysis to reveal the detailed structure of the corrosion product layer formed. As shown in Fig. 10, a very thin (about 100–200 nm) and porous layer of Fe_xS_y and Fe_xO_y was found on the steel surface. This layer was much thinner compared with the precipitated FeCO_3 layer typically observed in sweet corrosion (micron level), but still very thick compared with the passive layer on stainless steel (up to 5 nm). Most parts of the layers were detached from the substrate. Consequently, layer detachment alone cannot be used as an explanation for pit initiation.

TEM-EDS mapping results of the corrosion product layer on the 40 ppm H_2S specimen is shown in Fig. 11. In this 100–200 nm porous layer, iron, nickel, sulfur, and oxygen were concentrated, indicating the formation of sulfides and oxides.

Fig. 12 shows the EDS line scan result of the corrosion product layer

on the 40 ppm H_2S specimen. From the left side to the right side of the image, the very top layer was platinum coated for FIB cutting. Underneath was one layer of palladium, which was plated after the steel specimen was drawn out from the glass cell to prevent oxidation. Below these two plated layers, above the steel substrate, were corrosion product layers containing sulfur and oxygen. This result clearly shows that apart from sulfides or potentially elemental sulfur, oxides are an important part of the layer; especially the inner part of the layer near the steel surface. When and how these oxides were formed remained uncertain. Although further investigation was needed, SAED cannot provide phase identification information of the layers, only the diffraction pattern of the steel substrate was obtained. A meaningful diffraction pattern of the layer is very difficult to obtain because the layer is actually nanocrystalline with not enough lattice repeat units for X-ray diffraction [36]. Such layers can be considered as being “X-ray amorphous”.

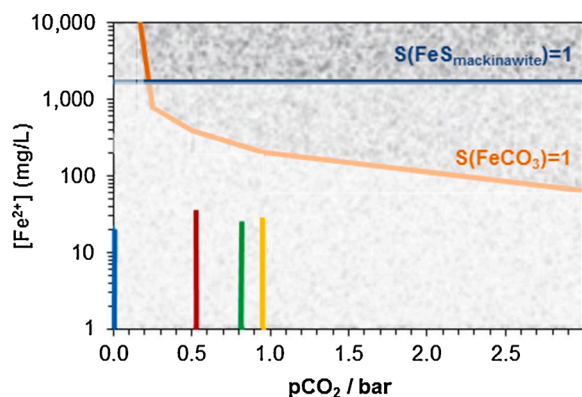


Fig. 13. Saturation degree of bulk solution for both $\text{FeS}_{\text{mackinawite}}$ and FeCO_3 for varied $p\text{CO}_2$. (X65 carbon steel, 30 °C, pH5, $p\text{CO}_2 = 0/0.53/0.82/0.97$ bar, $p\text{H}_2\text{S} = 0.04$ mbar, total pressure is 1 bar, the balance is N_2 , 1 wt.% NaCl, 300 rpm stir bar, $[\text{O}_2]_{\text{aq}} \approx 20$ ppb $_{(w)}$).

To summarize, the experimental results obtained at different H_2S partial pressures revealed that a thin FeS layer was responsible for a significant decrease in corrosion rate, as compared to the CO_2 only conditions. The general corrosion rates decreased with the increase of H_2S partial pressure. Localized corrosion happened when $0 < p\text{H}_2\text{S} < 150$ ppm $_{(v)}$. The pit initiation could have been related to the breakdown of the FeS layer formed under these conditions. The integrity of this protective layer seemed to be related to the partial pressure of H_2S , as no pitting was observed at $p\text{H}_2\text{S} = 150$ ppm $_{(v)}$. However, no clear correlation could be associated with the saturation degree of FeS in the bulk solution.

3.2. Effect of $p\text{CO}_2$ on pitting

The effect of $p\text{CO}_2$ on pitting in marginally sour environments was determined by running a series of experiments from 0 to 0.97 bar of CO_2 and at a fixed $p\text{H}_2\text{S} = 0.04$ mbar (40 ppm $_{(v)}$) with N_2 mixed as balance gas for a total pressure of 1 bar (atmospheric pressure). Fig. 13 shows the saturation degree for both FeS and FeCO_3 . In all of these experiments, the measured bulk ferrous ion concentration was always far lower than the concentration required to reach the saturation value of 1 for either S

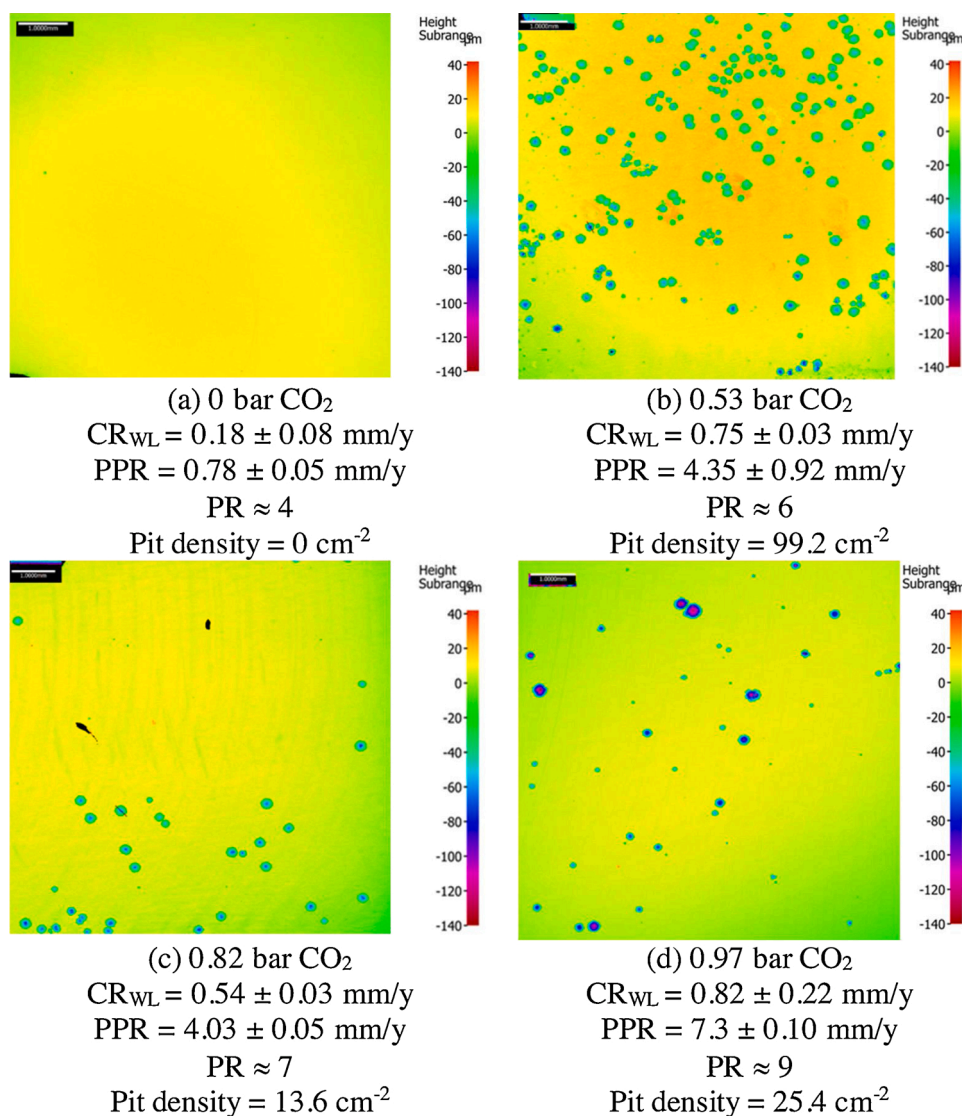


Fig. 14. Surface profilometry analysis of specimens recovered for each experimental condition after 7 days exposure after corrosion product layer removed. (X65 carbon steel, 30 °C, pH5, $p\text{CO}_2 = 0/0.53/0.82/0.97$ bar, $p\text{H}_2\text{S} = 0.04$ mbar, total pressure is 1 bar, the balance is N_2 , 1 wt.% NaCl, 300 rpm stir bar, $[\text{O}_2]_{\text{aq}} \approx 20$ ppb $_{(w)}$). The scales of the surface height of the three images were deliberately kept the same.).

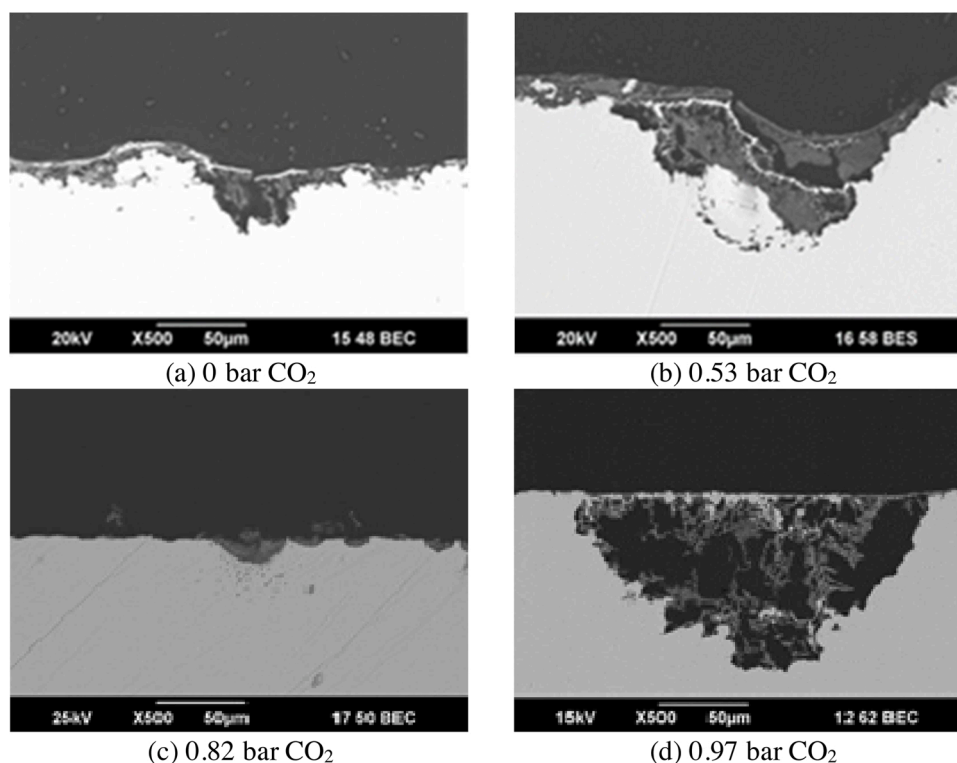


Fig. 15. SEM cross-section images of specimens at different CO_2 partial pressure after 7 days exposure. (X65 carbon steel, 30°C , pH_5 , $\text{pCO}_2 = 0/0.53/0.82/0.97$ bar, $\text{pH}_2\text{S} = 0.04$ mbar, total pressure is 1 bar, the balance is N_2 , 1 wt.% NaCl, 300 rpm, 7 days, $[\text{O}_2]_{\text{aq}} \approx 20$ ppb_w).

(FeS) or $\text{S(FeCO}_3)$. Consequently, no precipitation was expected in these experiments based on bulk water chemistry conditions.

The weight loss corrosion rate measurements in Fig. 14 show that any increase of CO_2 partial pressure generally leads to an increase of the general corrosion rates. The $\text{pCO}_2 = 0.53$ bar results were slightly higher than expected in this trend, although this experiment displayed higher pitting density (as shown in the next section); this could affect the average mass loss and consequently the general corrosion rate.

The profilometry images [Fig. 14 (b), (c) and (d)] show that pitting occurred in all the cases that contained CO_2 . Pitting densities are high under various partial pressures of pCO_2 . No clear trend could be detected between them [Fig. 14 (b), (c) and (d)]. This finding supports the hypothesis that pitting in marginally sour environments is related to pH_2S and probably a very thin FeS layer. However, the propagation rate of the pits seems to be related to pCO_2 , or to a larger extent to the overall corrosivity of the fluid, for the range of conditions used. This is demonstrated by the fact that pit penetration rates for $\text{pCO}_2 = 0.53$ bar and $\text{pCO}_2 = 0.82$ bar were smaller than in the 0.97 bar pCO_2 experiment.

Fig. 15 shows SEM cross-section images of specimens from experiments conducted at different pCO_2 values, where no distinct corrosion product layer can be seen on the surface of the steel. Although pitting initiation seems to be observed in the experiment conducted at $\text{pCO}_2 = 0$ bar [Fig. 15 (a)], the pit depth is too low (10–15 μm deep pits) to be truly characterized as pitting. In addition, specimens were retrieved after one, three- and seven-days exposure. The pit depths found on these samples were almost the same, and on the scale of surface roughness. Therefore, it can be deduced that at $\text{pCO}_2 = 0$ bar localized initiation may have happened, but no further propagation occurred. Similar results were previously reported by Fang, et al., in an H_2S only corrosion study [37]. This suggests that, in the experimental conditions selected for this study, pitting may initiate in the presence of H_2S , but does not propagate without CO_2 . For the specimens obtained at $\text{pCO}_2 = 0.53$ bar and $\text{pCO}_2 = 0.97$ bar, large pits were easily captured in the cross-sectional analysis. No pits were captured in the cross sections of the specimen from the $\text{pCO}_2 = 0.82$ bar CO_2 experiments, although there

could have been some, according to the surface profilometry results in Fig. 14 where pits are seen. The process of cross-sectioning a steel specimen does not always ensure that specific localized corrosion features will be captured, especially if the pitting density is low, since the specimen is cut at a random location.

Fig. 16, the TEM image for the $\text{pCO}_2 = 0$ bar experiment, reveals that, in H_2S only condition, a two-layer structure was formed. The total thickness of the two layers was about 500 nm. The layer seemed continuous and relatively dense. This layer offered some protection because: 1) the general corrosion rate was low (0.18 ± 0.08 mm/y); 2) no localized corrosion happened under this condition. Such a thick layer (compared with oxide layers or passive layers) was unexpected because the bulk solution was unsaturated with respect to mackinawite according to measurements of $[\text{Fe}^{2+}]$ and pH used for calculation of saturation degrees. Assuming that the layers were formed by precipitation, this indicated that the surface water chemistry was different from the bulk solution. Previous research findings in CO_2 only environments indicated that the surface pH value could be one to two units higher than that in the bulk solution [21,38].

TEM-EDS mapping results (Fig. 17) show that Fe, O, S, Ni elements were concentrated in the corrosion product layers. This indicates that sulfides and oxides were part of the composition of the corrosion product layers.

The TEM-EDS line scan results of the $\text{pCO}_2 = 0$ bar specimen are shown in Fig. 18. From the left side to the right side of the image, the very top layer corresponds to the platinum coating for FIB cutting. Underneath that layer was another coating of palladium, which was sputtered after the steel specimen was withdrawn from the glass cell to prevent oxidation. Below these two plated layers, above the steel substrate, were two layers containing sulfur and oxygen, indicating the possible existence of iron sulfide, as well as iron oxide or hydroxide. The outer layer was richer in elemental sulfur, while the inner layer was richer in element oxygen. The presence of oxygen is somehow unexpected. Nitrogen as a sparge gas was used to deaerate the aqueous solution for over two hours every time before the start of experiments, then

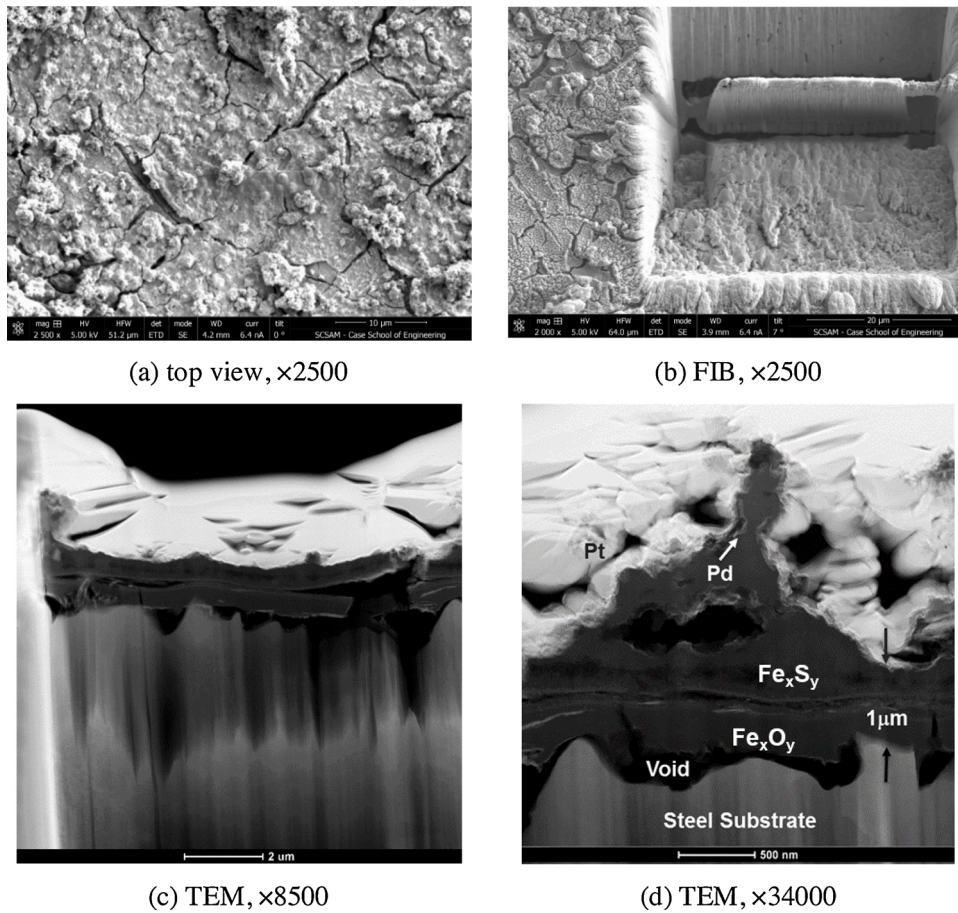


Fig. 16. TEM images of the cross section cut out by FIB from the specimen of H_2S/N_2 experiments. ($30\text{ }^\circ\text{C}$, $pN_2 = 0.97\text{ bar}$, $pH_2S = 0.04\text{ mbar}$, X65, pH 5, 1 wt.% NaCl, 300 rpm, 7 days, $[O_2]_{aq} \approx 20\text{ ppb}_{(w)}$).

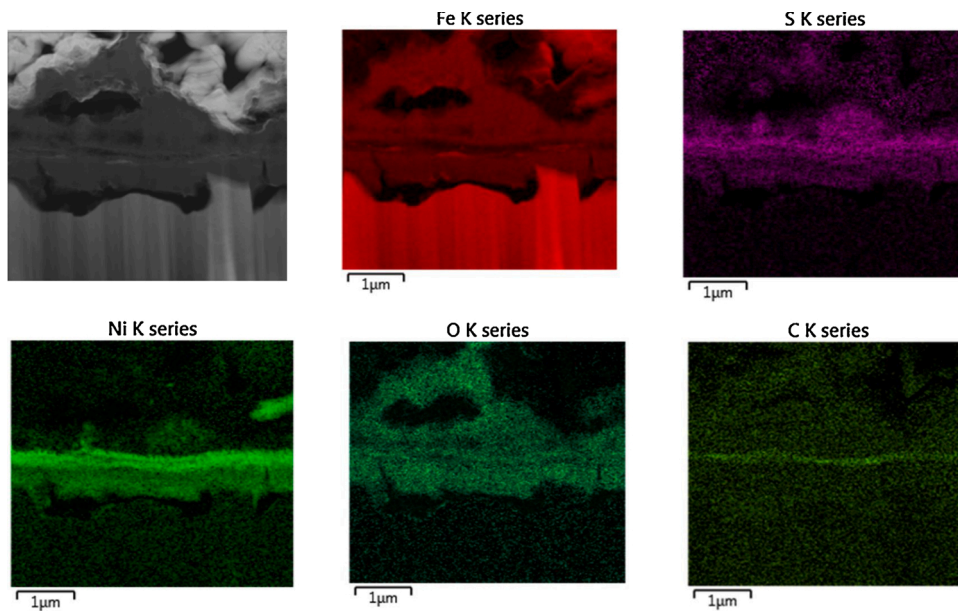


Fig. 17. TEM-EDS mapping results of the specimen of the H_2S/N_2 experiment ($pH_2S = 0.04\text{ mbar}$ and $pN_2 = 0.97\text{ bar}$, X65 carbon steel, $30\text{ }^\circ\text{C}$, pH 5, 1 wt.% NaCl, 300 rpm, 7 days, $[O_2]_{aq} \approx 20\text{ ppb}_{(w)}$).

N_2 and H_2S were bubbled in solution together for half an hour before the specimens were loaded. Consequently, it is not expected to retain significant dissolved O_2 in the environment (aqueous concentration of

oxygen in solution was measured at around $20\text{ ppb}_{(w)}$). Several explanations can be put forward to account for the presence of oxygen in the layer. The most logical one is that the layer could have been oxidized

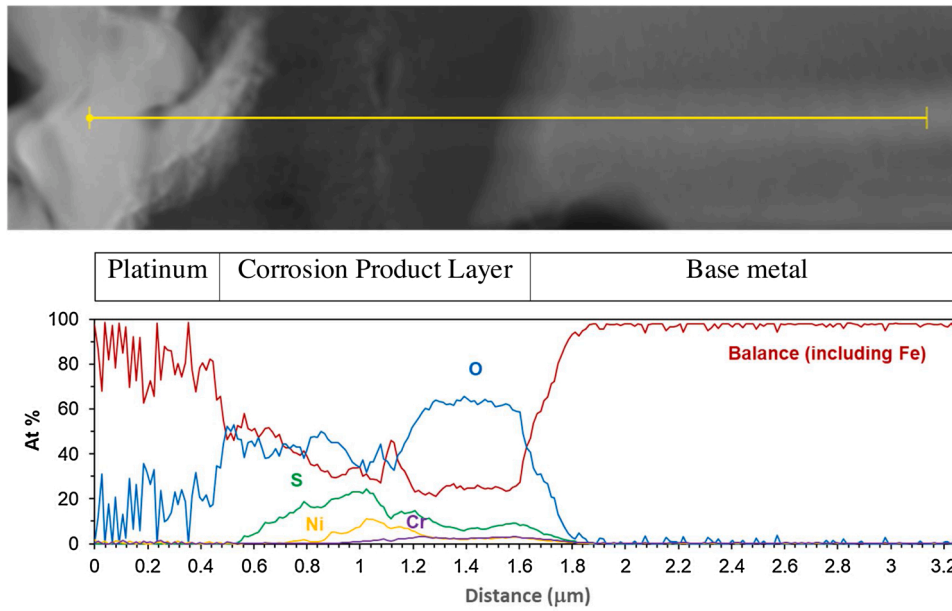


Fig. 18. TEM-EDS line scan results of the specimen of H₂S/N₂ experiment (30 °C, pH₂S = 0.04 mbar, pN₂ = 0.97 bar, X65 carbon steel, pH5, 1 wt.% NaCl, 300 rpm, 7 days, [O₂]_{aq} ≈ 20 ppb_(w)).

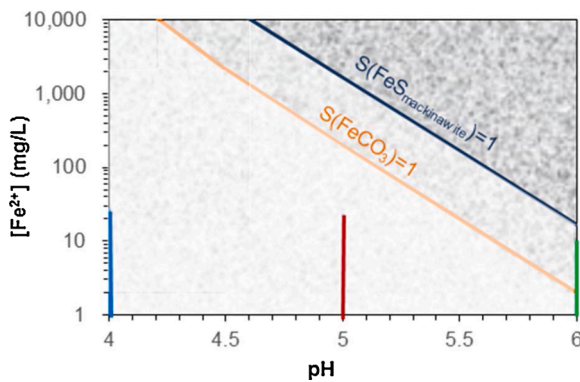


Fig. 19. Saturation degree of both FeS_{mackinawite} and FeCO₃ under various pH in the bulk solution. (X65 carbon steel, 30 °C, pH 4/5/6, pCO₂ = 0.97 bar, pH₂S = 0.04 mbar, 1 wt.% NaCl, 300 rpm, 7 days, [O₂]_{aq} ≈ 20 ppb_(w)).

during post-retrieval, during sample handling, storage and/or analysis. These scenarios are revisited in depth in the following part II of this series of research [39].

According to Table 3, manganese, nickel, and chromium are the most abundant alloying elements in the X65 steel specimen used in this study. However, only nickel was enriched in the two layers structure, especially in the upper layer. This enrichment of nickel could be due to the possible compound nickel sulfide (NiS) as it is found to be insoluble even in strong acid solutions [36,40,41].

It is clear from the experimental results that the presence of CO₂ is absolutely necessary for pitting initiation. Without CO₂, the FeS layer appears fairly protective while the added acidity due to the presence of H₂CO₃ appears to be related to layer damage and loss of protectiveness. At this point, it is hypothesized that the presence of any weak acid (in addition to H₂S_(aq)) is enough to increase the local surface H⁺ concentration, by dissociation, leading to local dissolution of the layer, preferential corrosion and pit initiation. In addition, galvanic corrosion could also be involved since the pit penetration rate seems to be higher than the corrosion rate typically experienced in CO₂-only environments

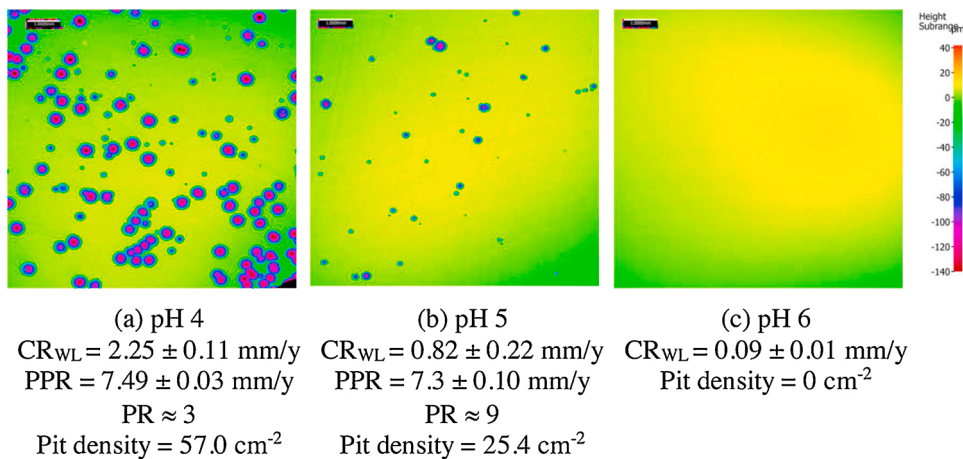


Fig. 20. Surface profilometry analysis at different pH after 7 days exposure after corrosion product layer was removed. Captions show the general corrosion rate as measured by weight loss (CR_{WL}), the Pitting Penetration Rate (PPR) and the Pitting Ratio (pH = 4/5/6, X65 carbon steel, 30 °C, pCO₂ = 0.97 bar, pH₂S = 0.04 mbar, 1 wt.% NaCl, 300 rpm stir bar, [O₂]_{aq} ≈ 20 ppb_(w)). The scales of the surface height of the three images were deliberately kept the same).

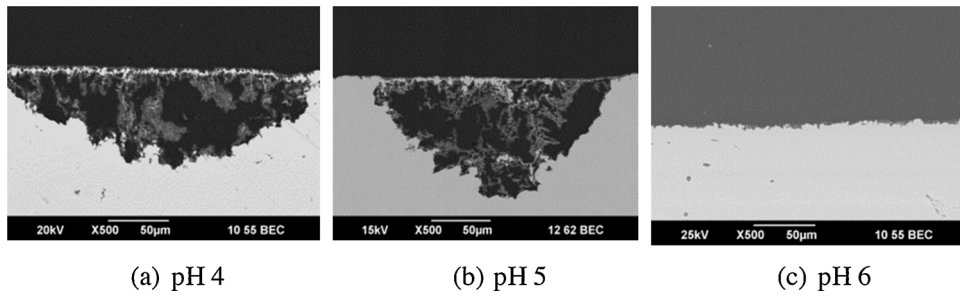


Fig. 21. SEM cross-section images at different pH after 7 days exposure. (pH = 4/5/6, X65 carbon steel, 30 °C, $p\text{CO}_2 = 0.97$ bar, $p\text{H}_2\text{S} = 0.04$ mbar, 1 wt.% NaCl, 300 rpm stir bar, $[\text{O}_2]_{\text{aq}} \approx 20$ ppb_(w)).

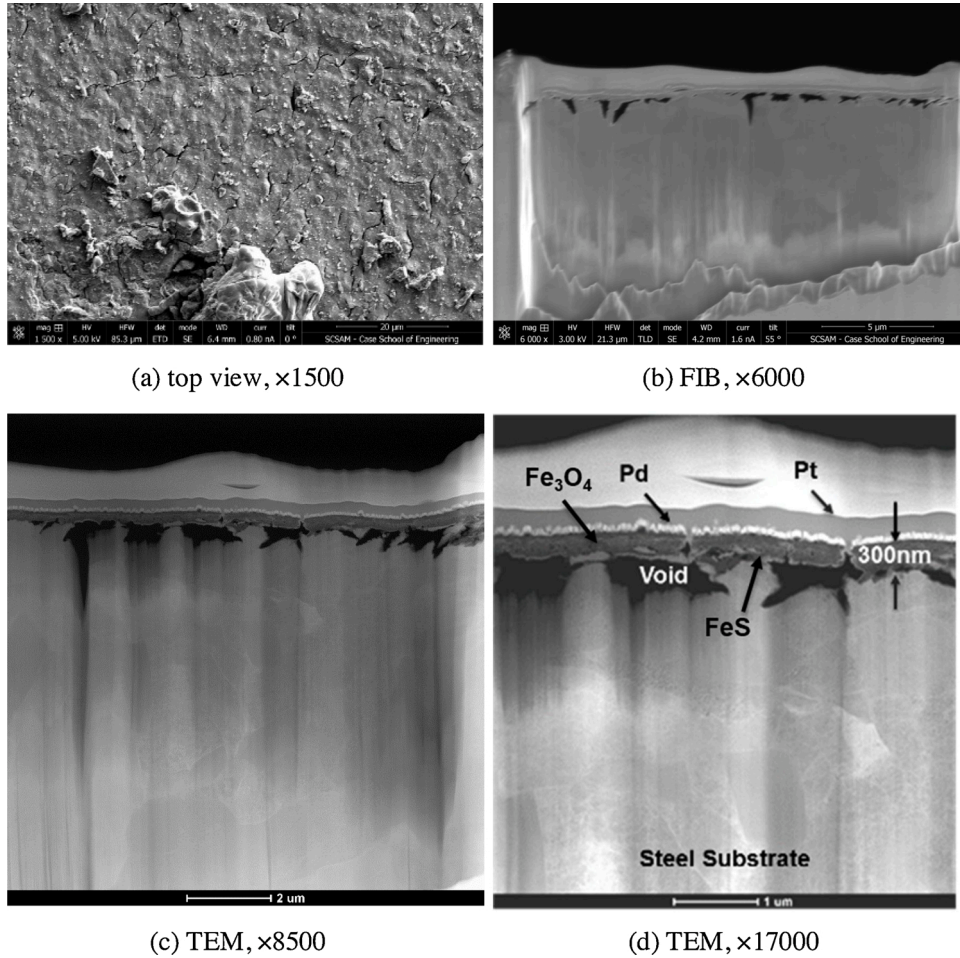


Fig. 22. TEM images of the cross section cut out by FIB from the specimen of pH 6 experiments. (30 °C, pH6, 0.97 bar CO_2 , 0.04 mbar H_2S , X65, 1 wt.% NaCl, 300 rpm, 7 days, $[\text{O}_2]_{\text{aq}} \approx 20$ ppb_(w)).

at the same pH value.

3.3. Effect of pH on pitting

The effect of pH on pitting in marginally sour environments was evaluated at pH 4, 5 and 6 in the bulk solution. The vertical lines shown in Fig. 19 represent the range of concentration of ferrous ions observed during each experiment. The saturation values for both FeS and FeCO_3 are dependent on solution pH value. Fewer ferrous ions were required to reach saturation at higher pH 6. Fig. 19 shows that both FeS and FeCO_3 were far from saturation in the experiments at pH 4 and pH 5. At pH 6, $S(\text{FeCO}_3)$ exceeded the saturation value of 1, while $S(\text{FeS})$ was very close to saturation, all based on bulk solution conditions. This indicates that

supersaturation with respect to both types of corrosion products was likely at the steel surface. Consequently, a protective corrosion product layer, composed of possibly both FeS and FeCO_3 , could have been expected in the pH 6 case.

Fig. 20 shows surface profilometry results done on specimens after removal of the corrosion product layer. Severe pitting is observed on the pH 4 specimen, accompanied by a very high general corrosion rate. Pitting density decreased significantly at pH 5, while the pit propagation rate remained almost the same. At pH 6, no pitting was detected and a very low general corrosion rate was measured. Weight loss corrosion rate measurements in Fig. 20 show the trend of the changes of general corrosion rates with pH: increased H^+ concentration leads to higher corrosion rates. Since pH is the logarithmic value of $[\text{H}^+]$, this change is

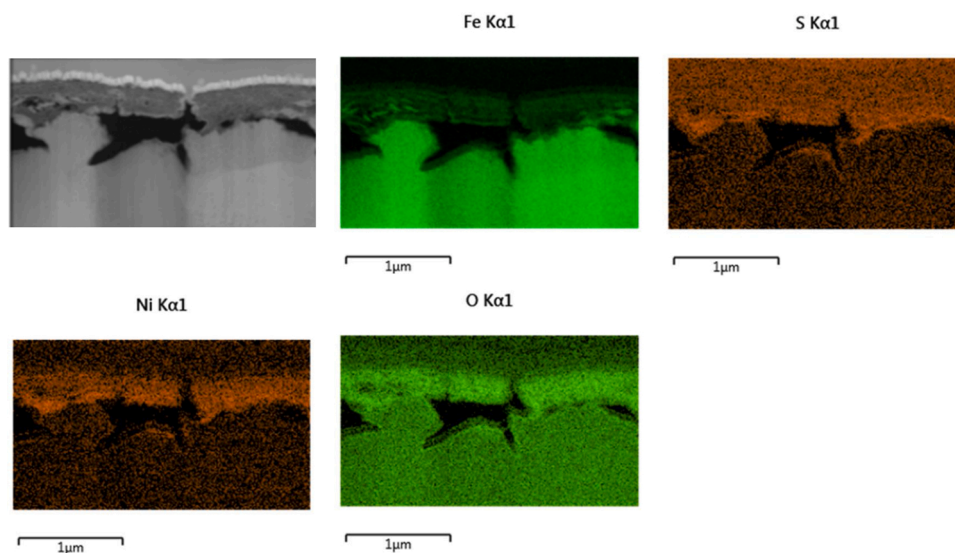


Fig. 23. TEM-EDS mapping results of the specimen of pH 6 experiment. (30 °C, 0.04 mbar H₂S and 0.97 bar CO₂, pH 5, 1 wt.% NaCl, 300 rpm, 7 days, [O₂]_{aq} ≈ 20 ppb_(w)).

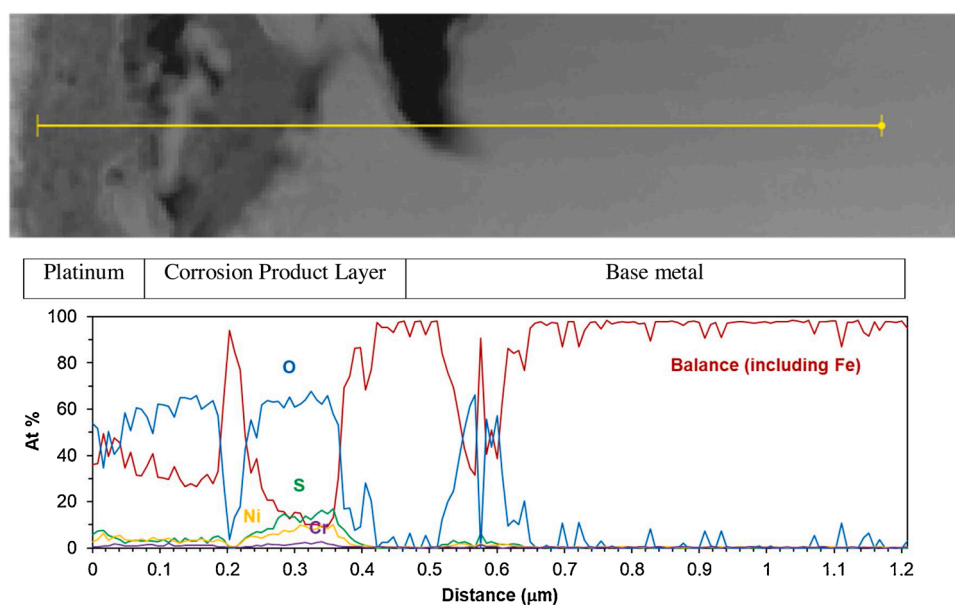


Fig. 24. TEM-EDS line scan results of the specimen pH 6 experiment. (30 °C, X65 steel, 0.04 mbar H₂S and 0.97 bar CO₂, 1 wt.% NaCl, 300 rpm, 7 days, [O₂]_{aq} ≈ 20 ppb_(w)).

drastic. This agrees with the saturation degree calculation results in Fig. 19. The scaling tendency (equation 8) also increased with increasing pH, which would indicate a more protective FeS layer at higher pH, with no pit initiation.

Cross-section images, shown in Fig. 21, indicate a high degree of pitting corrosion at pH 4 and 5, with similar pit depth in both cases. At pH 6, no pits are visible in the cross-section image, and this observation can be generalized over the entire specimen surface, as shown by profilometry analysis.

The corrosion product layer formed under the pH 6 condition, as shown in Figs. 22 and 23, is similar to that obtained at pH 5 (Figs. 10 and 11). This is somehow surprising as pitting occurred at pH 5 and not at pH 6; also, the general corrosion rate at pH 5 was higher than at pH 6 (0.82 mm/year at pH 5 compared to 0.09 mm/year at pH 6). Consequently, some differences in terms of corrosion product layer coverage, attachment and compactness are expected. It is possible that the random

selection of the location of the TEM analysis did not reflect these differences while they may appear on other locations. More striking differences exist between the compact layer obtained in H₂S-only environment (Fig. 16) and the seemingly more porous layer generated in systems containing both H₂S and CO₂, at pH 5 or 6 (Fig. 10 b and c). In the presence of CO₂, the dissociation of H₂CO₃ leads to a lower surface pH, which could be the reason for the lack of compactness and increased porosity of the corrosion products.

The explanation behind the absence of pitting at pH 6 could be linked to the surface pH, which is logically higher compared to pH 5. A higher surface pH represents a less aggressive environment and may also favor the formation of iron oxides or oxyhydroxides.

TEM-EDS line scan result of the specimen corresponding to the pH 6 experiment is shown in Fig. 24. This distribution of elements along the indicative line shows that the layer is comprised of Fe, O, S and Ni. This could infer the presence of iron oxides and sulfides in the layer (0.2 to

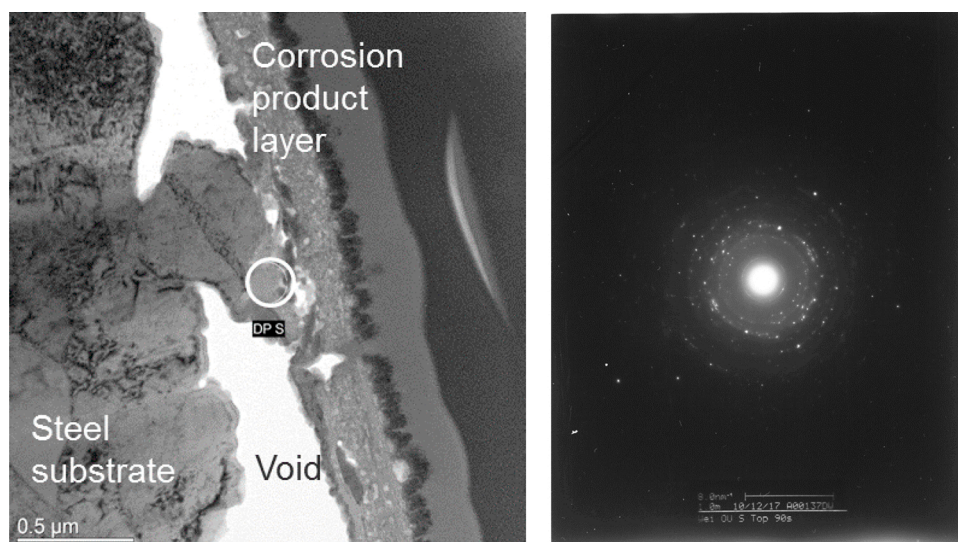


Fig. 25. TEM-SAED results near the inner layer of the specimen of pH 6 experiment. (30 °C, X65 steel, 0.04 mbar H₂S and 0.97 bar CO₂, 1 wt.% NaCl, 300 rpm, 7 days, [O₂]_{aq} ≈ 20 ppb_(w)).

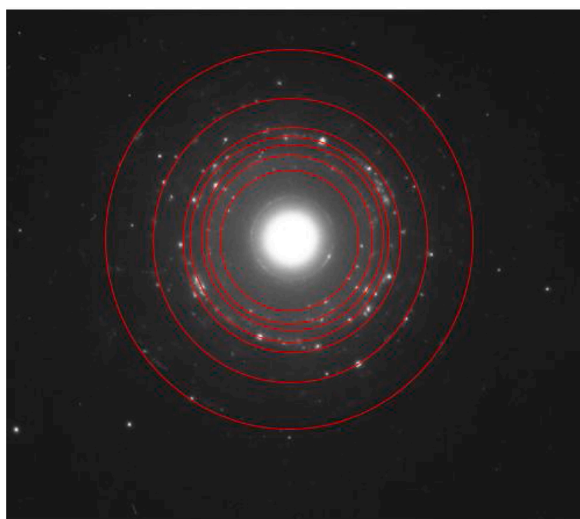


Fig. 26. Pattern analysis of the specimen of pH 6 experiment. (30 °C, X65 steel, 0.04 mbar H₂S and 0.97 bar CO₂, 1 wt.% NaCl, 300 rpm, 7 days, [O₂]_{aq} ≈ 20 ppb_(w)).

Table 5

Sulfide Analysis - Possible Match with Fe_{0.91}S.

| Ring number | Ring Diameter (nm ⁻¹) | Ring Radius (nm ⁻¹) | d Spacing (nm) |
|-------------|-----------------------------------|---------------------------------|----------------|
| 1 | 6.78 | 3.39 | 0.29 |
| 2 | 8.08 | 4.04 | 0.25 |
| 3 | 8.73 | 4.37 | 0.23 |
| 4 | 9.91 | 4.96 | 0.20 |
| 5 | 10.8 | 5.4 | 0.19 |
| 6 | 13.63 | 6.82 | 0.15 |
| 7 | 17.8 | 8.9 | 0.11 |

0.4 μm), although it is unclear at this point if the oxides were formed during the test or during post-processing and exposed to air. The coexistence of oxides and sulfides has been observed already for high temperature sour conditions [22], [42]: magnetite was formed due to reaction between steel and water, then the outer part of the layer was converted into iron sulfide. However, this work was done at low temperatures, direct reaction between steel and water vapor is less likely to

occur. Again, further studies and discussion about the existence of oxides will be one of the topics in the following part II of this research [39].

Fig. 25 shows the electron diffraction pattern (image on the right side) at the circled area near the inner layer in the image on the left side. The ring pattern is unfortunately not very clear but can be used to identify the polycrystalline sulfide compounds. The diameter of a ring is measured (Fig. 26) and converted to the d-spacing in real space between lattice planes. When comparing this pattern with the database of crystal diffractions, a possible match can be established with pyrrhotite (Fe_{0.91}S, Table 5), although mackinawite (FeS) was expected. The discrepancy can be explained by the fact that the first few molecular layers where nanocrystal mackinawite is supposed to form cannot be derived by the diffraction equation, which requires long-range order of the crystal structure repeat units [36].

Fig. 27 shows the precession electron diffraction (PED) acquired in the rectangular area. Each pixel on the map represents a square of 4 nm × 4 nm. The orientation map suggests that the crystal lattice parameter of the oxide compound was around 10 nm. Several iron sulfide phases (FeS, Fe₇S₈, etc., as listed in the upper right corner in Fig. 27) were selected for the data analysis. The colored map, in the lower right corner, suggests that mackinawite (FeS) is the most dominant iron sulfide present.

Fig. 28 shows the TEM-SAED results near the outer layer of the specimen corresponding to the pH 6 experiment. The diameter of a ring is measured and converted to the d-spacing in real space between lattice planes. Five rings were measured. They all match with magnetite very well. Therefore, the oxide formed near the outer layer can be identified as magnetite, Fe₃O₄.

In Fig. 29, a PED map (the image on the right side) was acquired in the rectangular area of the image on the left side. Each pixel in the map represents 10 nm. Both magnetite (Fe₃O₄) and hematite (Fe₂O₃) were used for data analysis, as listed in the upper right corner. The orientation map suggests the crystal size of the oxide is around 20 nm. The overlapped map in the lower right corner suggested that PED reliably identified Fe₃O₄. This agrees well with the previous SAED result.

In summary, pitting in marginally sour environments was observed at pH 4 and 5. Also, the tendency of occurrence of localized corrosion could be lowered by increasing the pH in the system. Phase identification by SAED and PED indicate that nanocrystalline mackinawite was the phase most likely present as the inner layer; the outer layer being composed of magnetite, as a possible product of mackinawite oxidation. However, when and how the oxidation of the outer layer happened

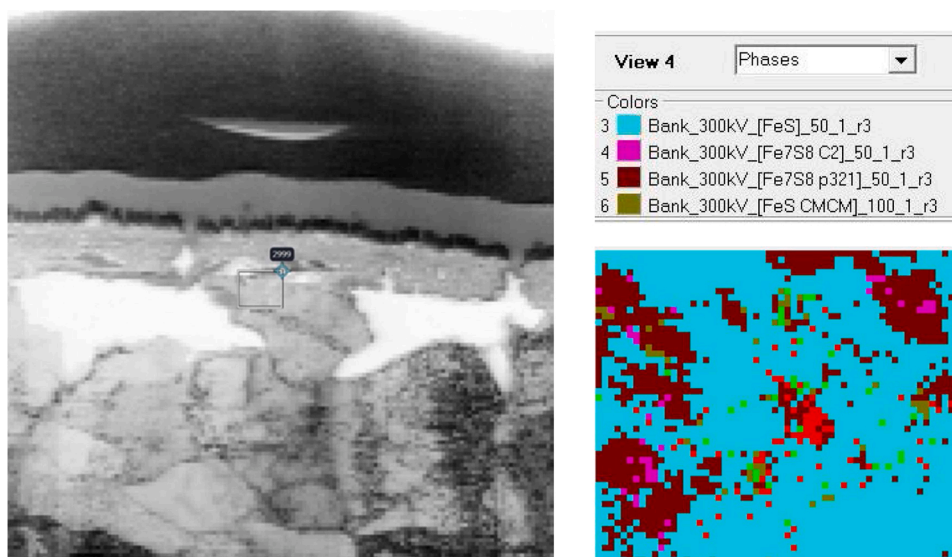


Fig. 27. Orientation/phase map by PED near the inner layer of the specimen of pH 6 sample. (30 °C, X65 steel, 0.04 mbar H₂S and 0.97 bar CO₂, 1 wt.% NaCl, 300 rpm, 7 days, [O₂]_{aq} ≈ 20 ppb_(w)).

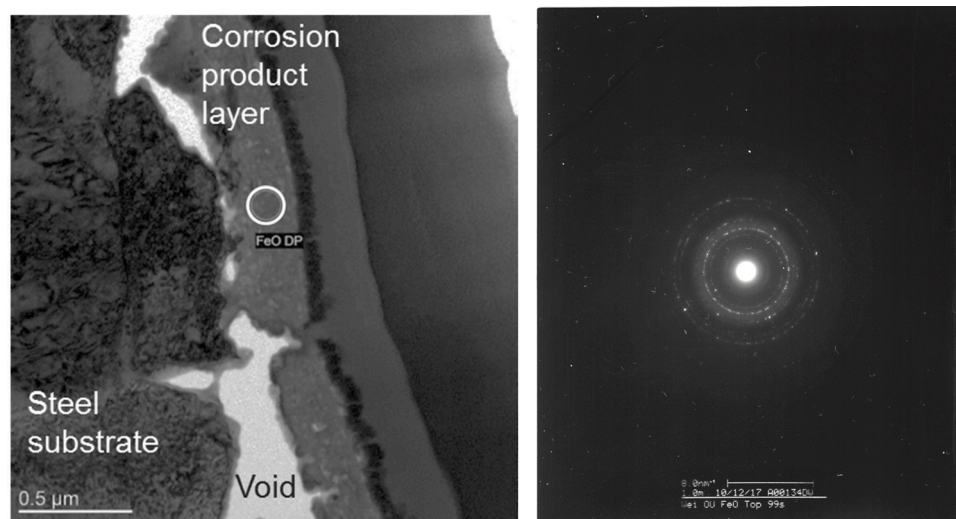


Fig. 28. TEM-SAED results near the outer layer of the specimen of pH 6 experiment. (30 °C, X65 steel, p_{H₂S} = 0.04 mbar, p_{CO₂} = 0.97 bar, 1 wt.% NaCl, 300 rpm, 7 days, [O₂]_{aq} ≈ 20 ppb_(w)).

remains unknown. Further investigation is required. The findings revealed that the presence of a buffering weak acid (H₂CO₃) seems to be related to a weakening of the protectiveness of the layer, at least at pH 5 and lower.

3.4. Effect of temperature on pitting

The effect of temperature on pitting was investigated at p_{H₂S} = 0.04 mbar (40 ppm) by performing experiments at 30 °C, 60 °C, and 80 °C. Since the experiments were conducted in a glass cell at atmospheric pressure (P_T = 1 bar), the changes in vapor pressure lead to different values of p_{CO₂} with temperature, from 0.97 bar at 30 °C, to 0.82 bar at 60 °C and 0.53 bar at 80 °C. The effect of pH to the saturation degree is more significant than the effect of [Fe²⁺]. Solution pH became difficult to control under elevated temperatures. Therefore, pH was recorded and compared at different temperatures in this case to make the comparison, rather than [Fe²⁺]. For the rest factors other than temperature, pH was kept as constant all the time. According to the water chemistry calculation for the bulk conditions, the solution was under-saturated with

respect to FeS and FeCO₃ in experiments at 30 °C, saturated only with respect to FeS at 60 °C, and saturated with respect to both FeS and FeCO₃ at 80 °C, as shown in Fig. 30. Based on the arguments developed above, one should expect localized corrosion to happen at 30 °C, probably not at 60 °C, and definitively no pitting was expected at 80 °C, due to high supersaturation with respect to both FeS and FeCO₃.

Surface profilometry shown in Fig. 31 clearly indicates that pitting was observed at 30 °C with a very high pit penetration rate, while at 60 °C and 80 °C the corrosion attack was extensive but uniform. The general corrosion rates increased dramatically as the temperature increased, which was also fully expected. As a rule of thumb, an increase of temperature by 10 °C leads to a doubling of the reaction rate.

Fig. 32 shows SEM cross-section images of specimens at different temperatures, which confirm the hypothesis based on saturation. At 30 °C, pitting is clearly detected, while at 60 °C, the surface morphology seems to indicate that pits initiated and then grew larger and agglomerated to form a uniformly rough surface. This is a typical description of uniform corrosion. At 80 °C, the morphology of the corrosion attack appeared different with a very rough surface but no distinct pitting.

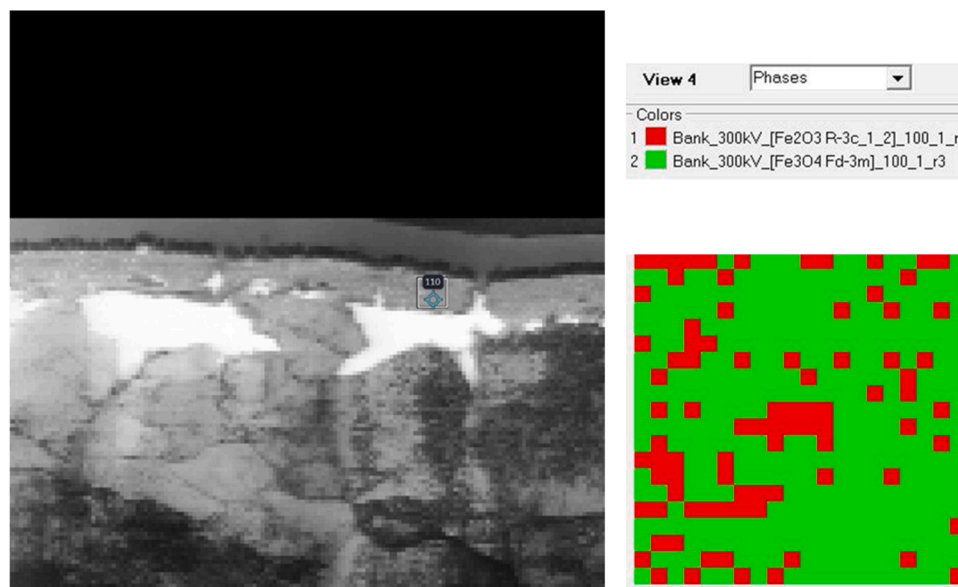


Fig. 29. Orientation/Phase Map by PED near the outer layer of the specimen of pH 6 experiment. (30 °C, X65 steel, 0.04 mbar H₂S and 0.97 bar CO₂, 1 wt.% NaCl, 300 rpm, 7 days, [O₂]_{aq} ≈ 20 ppb_(w)).

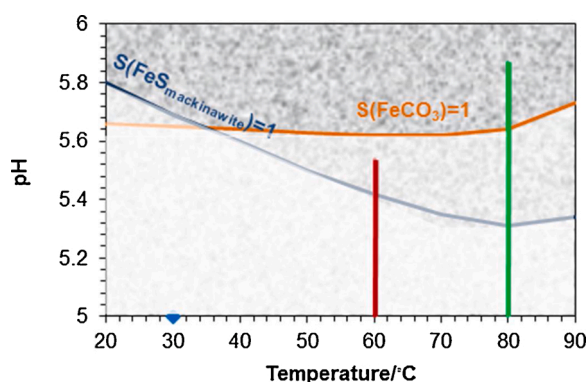


Fig. 30. Saturation degree of both FeSmackinawite and FeCO₃ at various temperatures in bulk solution. (X65 carbon steel, 30/60/80 °C, target pH 5, pCO₂ = 0.97/0.82/0.53 bar, pH₂S = 0.04/0.03/0.02 mbar, 1 wt. % NaCl, 300 rpm stir bar, 7 days, [O₂]_{aq} ≈ 20 ppb_(w)).

Pitting corrosion was only observed at 30 °C, while severe but uniform corrosion was experienced at higher temperatures. It is postulated that above 60 °C, the pitting density is so high that pits agglomerate rapidly leading to a uniformly corroded surface. In these conditions, the corrosion product layer is not protective. High temperature simultaneously accelerated both uniform corrosion and the pit initiation related reactions at the same time. At lower temperatures, localized corrosion is more likely to occur because the initiation sites are much fewer than at elevated temperatures. According to the rule of thumb of localized corrosion: “large cathode area, small anode area”, the less the pit initiates, the more dangerous it could be.

3.5. Effect of salt concentration on pitting

The effect of sodium chloride concentration on pitting was investigated at pH 5, pH₂S = 0.04 mbar (40 ppm) and pCO₂ = 0.97 bar by performing experiments without any NaCl and with adding 1 and 10 wt. % NaCl. The saturation degrees of FeS and FeCO₃ are illustrated in Fig. 33, which shows that both FeS and FeCO₃ are far from being saturated, over the whole range of bulk NaCl concentrations tested. Here, the saturation degree of FeS does not change with NaCl concentration

because neither the dissociation equilibrium constant equation [43] nor the solubility constant equation [44] of FeS includes dependence on the ionic strength. It is understood to be incorrect but no other expression of the equilibrium constants is available. This is not the case with FeCO₃ where both the solubility constant as well as the dissociation constants are a function of ionic strength (NaCl concentration) [45].

It should be noted that besides deionized water, about 20 mL of 0.1 M Na₂CO₃ was added into the solution of the 0 wt.% NaCl (blank) experiment for pH control purposes. Therefore, it was not strictly salt-free. As shown in Table 6, the ionic strength of the 0 wt.% NaCl solution with 20 mL of 0.1 M Na₂CO₃ is of the order of 10⁻⁶ compared with 10⁻² for the 1 wt.% NaCl solution. Therefore, the comparison between the two solutions is meaningful.

Surface profilometry scanning images of specimens exposed to different NaCl concentrations are shown in Fig. 34. As the concentration of NaCl increased, the pit density increased even if there was no significant change in pit penetration rates. The pitting density could be related to the conductivity of the solution. Higher salt concentrations made the galvanic coupling effect between the steel and iron sulfide layer stronger [21,23]. In summary, the presence of NaCl or Cl⁻ does not seem to directly affect layer protectiveness breakdown and the occurrence of pitting corrosion. It does have an effect on the extent of pitting, which can be linked to the enhancement of the galvanic coupling in the presence of highly conductive electrolyte. NaCl or Cl⁻ concentration is consequently not found to be a controlling parameter in the protective layer breakdown mechanism.

The highest general corrosion rate was obtained at 1 wt. % of NaCl; while the lowest was at 10 wt. % of NaCl. With the increase in NaCl concentration to 10%, the general corrosion rate decreased significantly, as was expected (from a previous experimental study by Fang et al. [46]). Increases in NaCl concentration, or by extension in any salt concentration, decreases the solubility of CO₂ and H₂S in water; a phenomenon called the “salting out” effect [47]. The presence of high salt content also renders the solution highly non-ideal, affecting the activity of ionic and dissolved species; and therefore, the physical properties of the solution. Elaborating on these phenomena is out with the scope of this study, the main purpose of this experimental series being to test if high NaCl contents affect the pitting tendency in marginally sour environments. As mentioned earlier, the presence of Cl⁻ is known to affect the protectiveness of passive films, but not in this case of pitting in marginally sour environments. In addition, increasing the

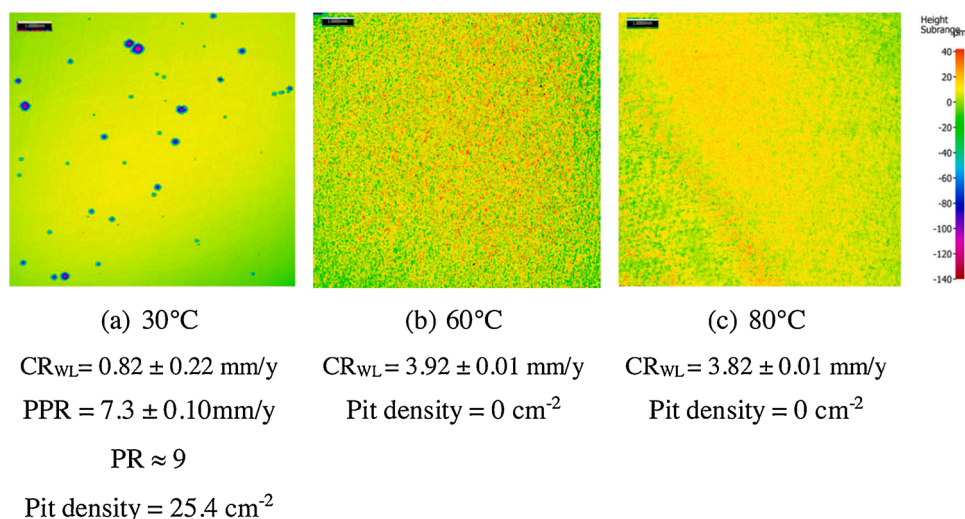


Fig. 31. Surface profilometry scanning images of different temperatures after 7 days exposure after corrosion product layer removed. (pH 5, X65 carbon steel, 30/60/80 °C, $pCO_2 = 0.97/0.82/0.53 \text{ bar}$, $pH_2S = 0.04 \text{ mbar}$, 1 wt.% NaCl, 300 rpm stir bar, $[O_2]_{aq} \approx 20 \text{ ppb}_{(w)}$). The scales of the surface height of the three images were deliberately kept the same.).

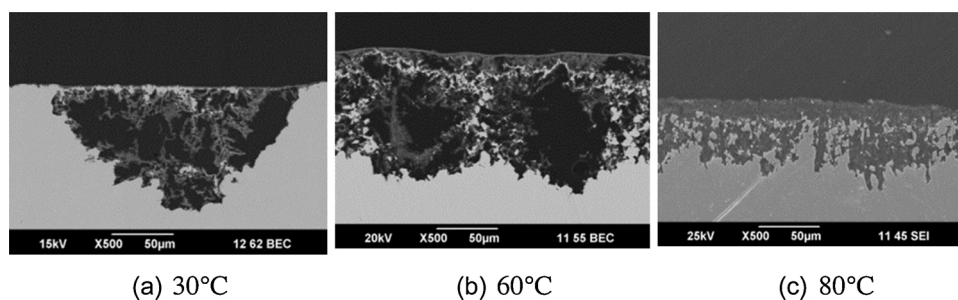


Fig. 32. SEM cross-section images of specimens at different temperatures after 7 days exposure. (X65 carbon steel, 30/60/80 °C, 0.97/0.82/0.53 bar CO_2 , pH 5, 1 wt.% NaCl, 300 rpm stir bar, $[O_2]_{aq} \approx 20 \text{ ppb}_{(w)}$).

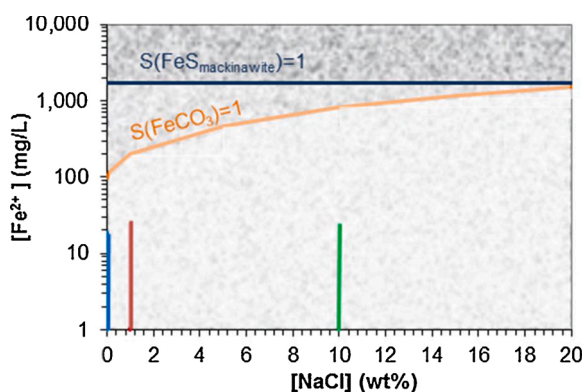


Fig. 33. Saturation degree of both $FeS_{mackinawite}$ and $FeCO_3$ of various salt concentrations in bulk solution. (X65 carbon steel, 30 °C, pH 5, $pCO_2 = 0.97 \text{ bar}$, $pH_2S = 0.04 \text{ mbar}$, 0/1/10 wt.% NaCl, 300 rpm stir bar, 7 days, $[O_2]_{aq} \approx 20 \text{ ppb}_{(w)}$).

ionic strength of the solution, and therefore its conductivity, could also enhance any galvanic corrosion if present.

SEM cross-section images of specimens at different NaCl concentrations are shown in Fig. 35. There does not seem to be a major difference in the pit morphology or depth with different NaCl concentrations, which is consistent with the reasoning presented above and the saturation calculations shown in Fig. 33.

Table 6

Ionic strength of solutions of various NaCl weight percentage.

| Weight percent | Concentration | Ionic strength | Salt |
|----------------|-----------------------|-----------------------|------------|
| 0.01% | 1.71×10^{-3} | 2.92×10^{-6} | NaCl |
| 0.1% | 0.0171 | 2.92×10^{-4} | NaCl |
| 1% | 0.171 | 0.0292 | NaCl |
| 10% | 1.71 | 2.92 | NaCl |
| 0.01% | 0.001 | 4×10^{-6} | Na_2CO_3 |

3.6. Summary of the information of layer composition provided by FIB-TEM

As summarized in Table 7, FIB-TEM, SAED, and PED analysis showed that a very thin layer of FeS, thought to be mackinawite, formed within the porous iron carbide network at the steel surface to retard general corrosion of the steel surface. Damage and breakdown of this thin FeS layer leads to pit initiation. This finding, together with the observation that no pitting happened without CO_2 , indicated that the pit propagated when the breakdown spots of the protective FeS layer were exposed to the H^+ buffering effect conferred by H_2CO_3 . Further pit propagation then followed due to galvanic coupling between the underlying steel and the conductive mackinawite corrosion product layer.

However, there was one key issue that made no sense: the co-existence of iron oxide with iron sulfide. It is considered that no oxide should be formed in a system that continuously sparging with H_2S because O_2 should be either purged out of the system or consumed by certain kinds of reducing reaction. However, there might be possibilities

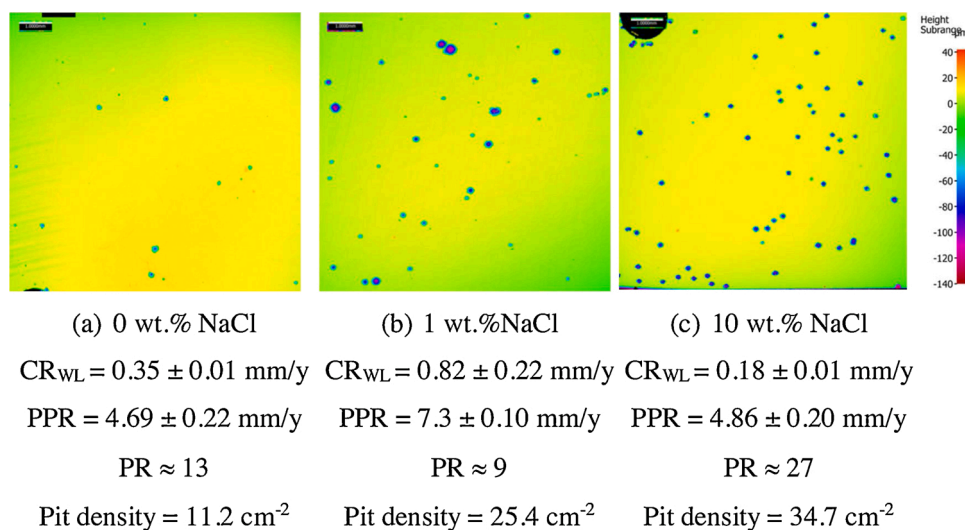


Fig. 34. Surface profilometry scanning images of specimens at different salt concentrations after 7 days exposure after corrosion product layer removed. (X65 carbon steel, 30 °C, pH5, $pCO_2 = 0.97$ bar, $pH_2S = 0.04$ mbar, 0/1/10 wt.% NaCl, 300 rpm stir bar, 7 days, $[O_2]_{aq} \approx 20$ ppb_(w)). The scales of the surface height of the three images were deliberately kept the same.)

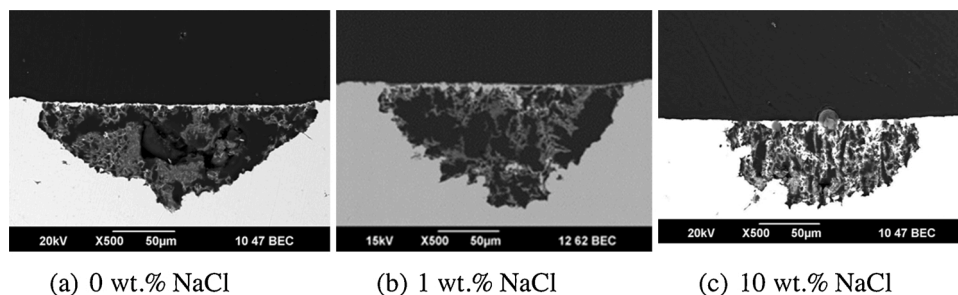


Fig. 35. SEM cross-section images of specimens at different salt concentrations after 7 days exposure. (X65 carbon steel, 30 °C, pH 5, 0.97 bar CO₂, $pH_2S = 0.04$ mbar, 0/1/10 wt.% NaCl, 300 rpm, 7 days, $[O_2]_{aq} \approx 20$ ppb_(w)).

Table 7

A Summary of FIB-TEM analysis of the product layer of the selected conditions related to the occurrence of localized corrosion. Iron oxides was found together with sulfides in the layer. (30 °C, $pH_2S = 0.04$ mbar, $[NaCl] = 1$ wt. %, 7 days).

| pH | 5 | 5 | 6 |
|--------------------------------|--|---|---|
| pCO_2 /bar | 0.97 | 0 | 0.97 |
| WE material | X65 (carbide) | X65 (carbide) | X65 (carbide) |
| Uniform or localized corrosion | Severe pitting | No pit | No pit |
| Layer thickness | 100–200 nm | 1 µm | 200–300 nm |
| Morphology: | Porous layers | Two-layer structure | Porous layers |
| Phase identification | Amorphous FeS and Fe _x O _y | Inner Fe _x O _y rich layer, 500 nm; Outer Fe _x S _y rich layer, 800 nm | Inner part of the layer: FeS; outer part of the layer: Fe ₃ O ₄ |

that either O₂ cannot be eliminated 100% by continuous sparging of H₂S, or O₂ is consumed by reaction with Fe, then oxides could be formed. Then, could H₂S react with these oxides and form iron sulfide or other sulfur-containing compounds? This problem could be answered by thermodynamic calculations based on the Gibbs free energies under specific conditions (e. g. temperature and pressures) and concentrations, which would be published at the same time as the third part of this series of pitting mechanism investigation [48]. More importantly, the relation between the presence of oxides as part of the composition of the protective corrosion product layer and the pit initiation mechanism in

marginally sour environments would be revealed after a series of carefully designed experiments, which would be published at the same time as the second part of this series of pitting mechanism investigation [39].

4. Conclusions

The experimental results clarified the effect of particular parameters on the occurrence of pitting in marginally sour environments. The most severe localized corrosion was found at 30 °C, 0.04 mbar H₂S and 0.97 bar CO₂, pH 5, 1 wt.% NaCl, 300 rpm, 7 days, $[O_2]_{aq} = 20$ ppb_(w), which is referred to as the baseline condition hereafter. Pitting was observed at the following conditions:

- 1) H₂S partial pressures of 0.02 to 0.09 mbar (but not at 0 mbar and 0.15 mbar);
- 2) CO₂ partial pressure of 0.53 to 0.97 bar (but not at 0 bar i.e. in pure H₂S solution);
- 3) pH 4 and 5 (but not at pH6);
- 4) 30 °C only (but not 60 or 80 °C);
- 5) NaCl concentrations from 0 to 10%;

The partial pressure of H₂S and CO₂, pH, temperature, and ionic strength all can affect the saturation degree of the FeS in solution. Pitting only initiated when H₂S was present in this system and propagated only when CO₂ was present. These were proven by the fact that: 1) no pitting was found in CO₂ only experiments; 2) localized corrosion initiated but never propagated in the H₂S only experiments.

Chloride concentration was not found to be related to pit initiation as pitting was found in experiments at 0 wt.% of NaCl. However, the pitting density seemed to increase with increase in NaCl content, inferring a process controlled at least in part by galvanic coupling.

Damage and breakdown of this thin FeS layer leads to pit initiation. Pit propagated when the breakdown spots of the protective FeS layer were exposed to the H⁺ buffering effect conferred by H₂CO₃. Further pit propagation then followed due to galvanic coupling between the underlying steel and the conductive mackinawite corrosion product layer.

However, despite all the above enlightening findings, there were several questions yet to be answered. The origin and effect of oxides or oxyhydroxides discovered by TEM-SAED in this system need further investigation. Answers to these unexplained observations could help to reveal the detailed pit initiation mechanism in marginally sour environments.

Funding

This work was supported by the corrosion center joint industry project; Institute for Corrosion and Multiphase Technology, Ohio University, 342 West State Street, Athens, OH, 45701, USA.

Data availability statement

The raw/processed data required to reproduce these findings cannot be shared at this time due to technical or time limitations. They are available to readers upon email request to the Institute of Corrosion and Multiphase Technology.

CRedit authorship contribution statement

Wei Zhang: Conceptualization, Methodology, Formal analysis, Investigation, Data curation, Writing - original draft, Visualization. **Bruce Brown:** Methodology, Resources, Writing - review & editing, Project administration. **David Young:** Methodology, Writing - review & editing. **Gheorghe Bota:** Methodology. **Srdjan Nestic:** Conceptualization, Methodology, Writing - review & editing, Funding acquisition. **Marc Singer:** Conceptualization, Methodology, Writing - review & editing, Supervision, Funding acquisition.

Declaration of Competing Interest

The authors report no declarations of interest.

References

- [1] S.N. Smith, M. Joosten, Corrosion of carbon steel by H₂S in CO₂ containing oilfield environments - 10 year update, in: NACE Corrosion Conf., Paper No. 5484, NACE, Houston, TX, USA, 2015.
- [2] J. Larsen, Downhole nitrate applications to control sulfate reducing bacteria activity and reservoir souring, in: NACE Corrosion Conf., Paper No. 02025, NACE, Houston, TX, USA, 2002.
- [3] S. Navabzadeh Esmaeely, W. Zhang, B. Brown, M. Singer, S. Nešić, Localized corrosion of mild steel in marginally sour environments, *Corros. J.* 73 (9) (2017) 1098–1106.
- [4] W. Yan, B. Brown, S. Nestic, Investigation of the threshold level of H₂S for pitting of mild steel in CO₂ aqueous solutions, in: NACE Corrosion Conf., Paper No. 11472, Phoenix, AZ, NACE, 2018.
- [5] N. Yaakob, Top of the Line Corrosion in CO₂/H₂S Environments, Ph.D. Dissertation, Dept. Chem. & Biomol. Chem. Eng., Ohio Univ., Athens, OH, 2014.
- [6] B. Brown, D. Young, S. Nešić, Localized corrosion in an H₂S / CO₂ environment. International Corrosion Congress/17, NACE, Houston, TX, 2009.
- [7] N. Yaakob, F. Farel, M. Singer, S. Nestic, D. Young, Localized top of the line corrosion in marginally sour environments, in: NACE Corrosion Conf., Paper No. 96026, NACE, Houston, TX, USA, 2016.
- [8] J.R. Galvele, Transport processes and the mechanism of pitting of metals, *J. Electrochem. Soc.* 123 (1976) 464–474.
- [9] D.D. Macdonald, The point defect model for the passive state, *J. Electrochem. Soc.* 139 (1992) 3434–3449.
- [10] H. Strehlow, Mechanisms of pitting corrosion, in: P. Marcus (Ed.), *Corrosion Mechanisms in Theory and Practice*, Marcel Dekker, Inc., 2002.
- [11] A. Dugstad, Mechanism of protective film formation during CO₂ corrosion of carbon steel, in: NACE Corrosion Conf., Paper No. 31, NACE, Houston, TX, USA, 1998.
- [12] Y. Sun, Localized CO₂ corrosion in horizontal wet gas flow, Ph.D. dissertation, Dept. Chem. & Biomol. Chem. Eng., Ohio Univ., Athens, OH, 2003, pp. 31–32.
- [13] D. Rickard, G.W. Luther III, Chemistry of iron sulfides, *Chem. Rev.* 107 (2007) 514–562.
- [14] D.W. Shoesmith, M.G. Bailey, B. Ikeda, Electrochemical formation of mackinawite in alkaline sulphide solutions, *Electrochim. Acta* 23 (1978) 1329–1339.
- [15] W. Sun, S. Nestic, A mechanistic model of uniform hydrogen sulfide/carbon dioxide corrosion of mild steel, *Corros. J.* 65 (2009) 291–307.
- [16] Y. Zheng, J. Ning, B. Brown, S. Nešić, Advancement in predictive modeling of mild steel corrosion in CO₂- and H₂S-containing environments, *Corros. J.* 72 (2016) 679–691.
- [17] P. Marcus, E. Protopopoff, Potential-pH diagrams for adsorbed species, application to sulfur adsorbed on iron in water at 25 °C and 300 °C, *J. Electrochem. Soc.* 137 (9) (1990) 2709–2712.
- [18] D.E. Jiang, E.A. Carter, Adsorption, diffusion, and dissociation of H₂S on Fe (100) from first principles, *J. Phys. Chem. B* 108 (2004) 19140–19145.
- [19] Z. Ma, Y. Yang, B. Brown, S. Nestic, M. Singer, Investigation of FeCO₃ and FeS precipitation kinetics by EQCM, in: NACE Corrosion Conf., Paper No. 11192, NACE, Houston, TX, USA, 2018.
- [20] S. Gao, P. Jin, B. Brown, D. Young, S. Nestic, M. Singer, Corrosion behavior of mild steel in sour environments at elevated temperatures, *Corros. J.* 73 (8) (2017) 915–926.
- [21] J. Ning, Y. Zheng, B. Brown, D. Young, S. Nestic, The role of iron sulfide polymorphism in localized H₂S corrosion of mild steel, *Corros. J.* 73 (2016) 155–168.
- [22] S. Gao, B. Brown, D. Young, M. Singer, Formation of iron oxide and iron sulfide at high temperature and their effects on corrosion, *Corros. Sci.* 135 (2018) 167–176.
- [23] S. Navabzadeh, G. Bota, B. Brown, S. Nešić, Influence of pyrrhotite on the corrosion of mild steel, *Corros. J.* 74 (2017) 37–49.
- [24] J. Han, S. Nestic, Y. Yang, B.N. Brown, Spontaneous passivation observations during scale formation on mild steel in CO₂ brines, *Electrochim. Acta* 56 (2011) 5396–5404.
- [25] G. Genchev, A. Erbe, Raman spectroscopy of mackinawite FeS in anodic iron sulfide corrosion products, *J. Electrochem. Soc.* 163 (6) (2016) C333–C338.
- [26] E. van Hunnik, B.F.M. Pots, E.L.J.A. Hendriksen, The formation of protective FeCO₃ corrosion product layers in CO₂ corrosion, in: NACE Corrosion Conf., Houston TX, NACE International, 1996 paper no. 6.
- [27] J. Han, Galvanic Mechanism of Localized Corrosion for Mild Steel in Carbon Dioxide Environments, Ph.D. dissertation, Dept. Chem. & Biomol. Chem. Eng., Ohio Univ., Athens, OH, 2009.
- [28] API Specification 5L: Specification for Line Pipe, forty-third edition, 2004. March 2004. Effective Date: October 2004 Errata December.
- [29] Test report, method: Fe-10-M, Type Standard: N-NIST-1763a, 2014 by Laboratory testing inc. May 14.
- [30] A.A. Al-Asadi, Iron Carbide Development and Its Effect on Inhibitor Performance, Master's Thesis, Ohio University, 2014.
- [31] X. Zhong, B. Brown, W. Li, S. Nestic, M. Singer, How to maintain a stable solution chemistry when simulating CO₂ corrosion in a small volume laboratory system, in: NACE Corrosion Conf., Paper No.7780, NACE, Houston, TX, USA, 2016.
- [32] B. Brown, The likelihood of localized corrosion in an H₂S/CO₂ environment, in: NACE Corrosion Conf., Paper No. 5855, NACE, Houston, TX, USA, 2015.
- [33] Hazards of Hydrogen Sulfide, Occupational Safety and Health Administration (OSHA), US Department of Labor, 2020. Retrieved on Dec 20, <https://www.osha.gov/hydrogen-sulfide/hazards>.
- [34] M. Nordsveen, S. Nestic, R. Nyborg, A. Stangeland, A mechanistic model for carbon dioxide corrosion of mild steel in the presence of protective ironcarbonate films—Part I: theory and verification, *Corrosion* (59) (2012) 443–456.
- [35] W. Zhang, Initiation and Propagation of Localized Corrosion of Mild Steel in Marginally Sour Environments, PhD Dissertation, Ohio University, 2020.
- [36] D. Rickard, G.W. Luther III, Chemistry of iron sulfides, *Chem. Rev.* 107 (2007) 514–562.
- [37] H. Fang, B. Brown, S. Nešić, Effects of sodium chloride concentration on mild steel corrosion in slightly sour environments, *Corros. J.* 67 (2011), 015001-1-015001-12.
- [38] J. Han, B.N. Brown, D. Young, S. Nestic, Mesh-capped probe design for direct pH measurements at an actively corroding metal surface, *J. Appl. Electrochem.* 40 (2010) 683–690.
- [39] Zhang W., Young D., Brown B. and Singer M., Pitting of mild steel in marginally sour environments – Part II: pit initiation based on the oxidation of the chemisorbed FeS layers, to be published in the same journal.
- [40] Nickel sulfide, prepared by an international group of experts on behalf of ILO and WHO, with the financial assistance of the European Commission. © ILO and, WHO (2017). http://www.ilo.org/dyn/icsc/showcard.display?p_card_id=0928.
- [41] A. Thiel, H. Gessner, The peculiarity of nickel and Cobalt Sulphides (Über Nickelsulfid und Kobaltsulfid. I. Die scheinbare Anomalie im Verhalten des Nickelsulfids gegen Säure), *J. Inorganic Gen. Chem. (Zeitschrift für anorganische Chemie)* 86 (May (1)) (1914) 1–57.
- [42] P. Jin, G. Bota, W. Robbins, S. Nestic, Analysis of oxide scales formed in the naphthenic acid corrosion of carbon steel, *Energy Fuels* 30 (8) (2016) 6853–6862.
- [43] Y.K. Kharaka, W.D. Gunter, P.K. Aggarwal, E.H. Perkins, J.D. DeBaal, Solmineq 88: a Computer Program for Geochemical Modeling of Water Rock Interactions, Alberta Research Council, Menlo Park, CA, 1989.

- [44] M. Bamberg, Gmelin handbuch der anorganischen chemie, schwefel, in: A. Teil (Ed.), Lieferung 3, VCH, Weinheim, 1953, p. 1959. Dissertation, Univ. Saarbrücken.
- [45] M. Nordsveen, S. Nesić, R. Nyborg, A. Stangeland, A mechanistic model for carbon dioxide corrosion of mild steel in the presence of protective iron carbonate Films—part 1: theory and Verification, *Corrosion* 59 (2003) 443–456.
- [46] H. Fang, B. Brown, S. Nesić, Sodium chloride concentration effects on general CO₂ corrosion mechanisms, *Corros. J.* 69 (2013) 297–302.
- [47] D. Koschel, J.-Y. Coxam, V. Majer, Enthalpy and solubility data of H₂S in aqueous salt solutions at conditions of interest for geological sequestration, *Ind. Eng. Chem. Res.* 52 (2013) 14483–14491.
- [48] Zhang W., Brown B., Young D., Smith S., Huizinga S., Singer M., Pitting of mild steel in marginally sour environments – Part III: Pit Propagation based on Acidification by Catalytic Oxidation of Dissolved Hydrogen Sulfide, to be published.